A synthetic phase-contrast imaging diagnostic with spatial filtering for gyrokinetic simulations

A. Iantchenko,[1] S. Coda,[1] S. Brunner,[1] G. Merlo,[2] J. Ball,[1] and F. Margairaz[3]

[1)]*Ecole Polytechnique Fédérale de Lausanne (EPFL), Swiss Plasma Center (SPC), CH-1015 Lausanne, Switzerland*

[2)]*University of Texas at Austin, Austin, United States*

[3)]*University of Utah, Department of Mechanical Engineering, Salt Lake City, United States*

A Phase-Contrast Imaging (PCI) diagnostic provides measurements of line-integrated electron density fluctuations. Localisation along the laser beam path can be achieved with a spatial filter that selects the wave-vector directions of the fluctuations contributing to the PCI measurement, and is a key feature of the PCI diagnostic installed on the TCV tokamak and also of a similar system planned for JT-60SA. We have developed a synthetic diagnostic that models measurements from PCI taking into account the effect of such a spatial filter. The synthetic tool is based on the principle of integrating over selected diagnostic volumes the electron density fluctuations generated by turbulence simulations, and applying an appropriate spatial filter in wave-vector space. We demonstrate the effect of the filter for a positive and a negative triangularity TCV discharge, and illustrate the potential of the synthetic diagnostic for better understanding the corresponding experimental results. We consider different types of filters and make first-principle estimates of the localisation of the measurement. Finally, using gyrokinetic simulations that include electromagnetic effects, collisions and four kinetic species, we make first predictions of the characteristics of the measurements using the planned set-up of PCI on JT-60SA.

I. INTRODUCTION

Turbulence driven by small scale instabilities causes significant transport of heat and particles, greatly reducing the confinement time and preventing the formation of a self-sustained plasma reaction in magnetic confinement devices. Mitigation of this transport is crucial to achieve controlled fusion, which requires a proper understanding of the underlying physics of the turbulent processes.

For a systematic study of turbulence phenomena one should take both a theoretical and an experimental approach. Theory is necessary for understanding and predicting turbulence phenomena, which, due to their complexity, often involves carrying out numerical simulations and modelling. While this approach gives an understanding of turbulence from first principles physics it often relies on assumptions and simplifications of the real-life event. To ensure that the simplified models are valid and the theoretical predictions are accurate, the modelled turbulence should be compared with experimental measurements of the fluctuating quantities. Apart from validating the theory such a comparison, just as importantly, helps to interpret experimental measurements that are often complex and difficult to link to the underlying physical mechanisms. For example measurements can give information on fluctuations integrated over a laser beam path or the change in the shape of a pulse after being reflected by the turbulent structures, thus providing an indirect observation of the underlying turbulence. The result is also dependent on the measurement system geometry and procedure (such as optical components, passage of a laser beam through the plasma, etc.), and includes the combined effect of a range of fluctuation contributions. This is especially true for Phase-Contrast Imaging (PCI)[1–6], which provides information on small-scale electron-density fluctuations, integrated along the path of a laser beam that is injected through the plasma. The measure-

ment is an average over various fluctuation contributions, including for example those driven by the Ion Temperature Gradient (ITG) or Trapped Electron Modes (TEM) or caused by Geodesic Acoustic Modes (GAM). Distinguishing the contributions from the different type of modes is difficult, and further complicated by the effect of the measurement geometry and the optical set-up of the diagnostic. PCI measurements would therefore strongly benefit from a careful comparison with simulations.

A proper comparison between simulations and experiments should consist of two steps. The first is to generate realistic fluctuations accounting for plasma geometry and profiles from the corresponding experiment. Nowadays, several gyrokinetic codes[7–11] are able to compute turbulent fluctuations including multiple kinetic species, collisions and electromagnetic fields as well as experimental MHD geometry and global effects. The second step is to also model the experimental measurement procedure through a synthetic diagnostic that takes into account the exact measurement geometry and the response of diagnostic set-up and optical equipment. The same analysis procedures can then be applied to both the output of the synthetic diagnostic and the corresponding experimental data, so that valid one-to-one comparisons between the two can be made. In this paper we present the details of a synthetic diagnostic that has been developed to model measurements from PCI, by post-processing non-linear flux-tube gyrokinetic simulations performed with the Eulerian (grid-based) GENE code[7,12–15]. Synthetic PCI diagnostics have been developed and tested in the past[16–18], but a novel key element included in this paper is the effect of a spatial filter that is used in experiments to select preferential wave vector components that contribute to the measurement. Since the measured wave vector rotates along the laser beam path, the filter leads to a localisation of the PCI signal. Optimal localisation is achieved for a tangentially propagating PCI beam (i.e approximately tan-
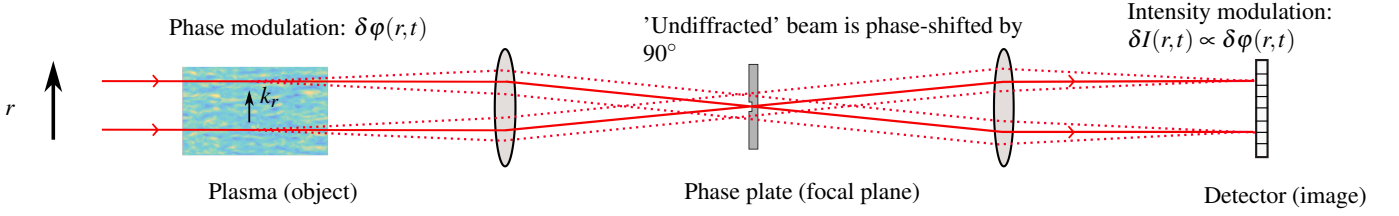
FIG. 1. Principles of PCI.

gential to the magnetic field), such as the Tangential Phase-Contrast Image (TPCI) diagnostic installed on TCV and the one planned for JT-60SA. In this paper we present the implementation of such a filter and the effect it has on the TPCI measurement. As an illustrative example we apply the synthetic diagnostic to two TCV discharges with different plasma triangularity. We also illustrate the features of the TPCI system planned for JT-60SA, using the output from relatively simple electromagnetic non-linear gyrokinetic simulations.

The remainder of this paper is organised as follows. First, in Section II we present the concept of the turbulence measurement with PCI and the principles of a spatial filter. In Section III we then explain the principle of the synthetic diagnostic, including details of the positive and negative triangularity discharges considered in this paper, and the implementation of a spatial filter. In Section IV we illustrate the effects of the spatial filter and compute the localisation from first principles. Finally, in Section V we apply the synthetic tool to interpret measurements of the positive and negative triangularity TCV discharges and make first predictions for PCI measurements on JT-60SA, before offering a conclusion in Section VI. Note that throughout this paper the subscript $\perp, 0$ refers to a wave vector perpendicular to the laser beam while $\perp, B$ refers to the wave vector perpendicular to the magnetic field.

II. THE PCI DIAGNOSTIC

The principle of phase-contrast imaging is depicted schematically in Fig. 1. We consider a laser beam with a frequency ω much larger than the electron plasma frequency and the electron gyration frequency, and a wavelength λ shorter than the scale of the density fluctuations in the plasma. Under these conditions, when a laser beam is sent through a plasma, the amplitude and shape of the beam are preserved, but variations in the refractive index introduce a small phase shift $\delta\varphi$ that is proportional to the line integral of the density fluctuations over the beam path L, according to the relation

$$\delta\varphi = r_e \lambda_0 \int_L \delta n_e \, d\ell, \tag{1}$$

where λ_0 is the laser wavelength and r_e is the classical electron radius[2]. In addition to the phase shift $\delta\varphi$ due to fluctuations ($|\mathbf{k}| > 0$) there is also a phase shift due to the slow spatial variation in the background density ($|\mathbf{k}| \approx 0$). Let $\varphi = \varphi_0 + \delta\varphi$ be the total phase shift imparted on the laser beam. We assume that $\delta\varphi \ll \varphi_0$. The electric field of the scattered laser

beam wave can be represented by

$$E_s = E_0 e^{i\delta\varphi} \sim E_0(1 + i\delta\varphi) \tag{2}$$

where we expanded to first order in $\delta\varphi$, and where the phase shift due to variation in the background density, φ_0, has been reabsorbed in the electric field component $E_0 = E_i \exp i\varphi_0$, where E_i is the incident electric field. If the scattered and unscattered components are directly recombined on an image plane, a set of square-law detector elements would measure an amplitude $|E_s| = E_i$, which is independent of the fluctuating phase shift that we try to quantify. However, if the unscattered components of the wave could be phase-shifted by 90° with respect to the scattered components, the total scattered field becomes

$$E_s = iE_0 + iE_0\delta\varphi, \tag{3}$$

and the intensity is then a function of $\delta\varphi$

$$|E_s|^2 \sim |E_0|^2(1 + 2\delta\varphi). \tag{4}$$

In this case, by recombining the scattered and unscattered components in an image plane, the temporal and spatial variation of the phase shift is transformed linearly into a measurable intensity modulation.

The phase shift can in practice be effected since the scattered and phase shifted components travel at a small angle to the laser beam propagation direction. A transmitting or reflecting optic, termed a *phase plate*[1,19] placed in the focal plane of a lens, can therefore be used to phase-shift the two components of the laser beam relative to each other. Such a phase plate is simply a mirror with a groove of $\lambda_0/8$ depth at the optical axis. A lens placed after the object causes the unscattered component affected by electron density fluctuations to pass though the optical axis on the focal plane, and into the groove, while scattered components are focused onto a distance $\delta x = F\mathbf{k}/k_0$ from the optical axis, where k_0 is the laser wave number and F is the focal length. This is illustrated in Fig. 1. Contrast is achieved by using a partially reflecting material for the groove which decreases the amplitude of the unscattered part of the wave by a factor $\sqrt{\rho}$ such that the measured intensity becomes $|E_0|^2(\rho + 2\sqrt{\rho}\varphi)$, and contrast has been enhanced by $\sqrt{\rho}$.

The width of this groove needs to be large enough to accommodate the full diffraction spot of the unscattered component. The diffraction limited focal point is $\sim (F/a)\lambda_0$, where a is the optical aperture, and is typically $0.15 - 0.5$ mm wide in practical applications, for the most commonly used laser wavelength, $10.6\ \mu$m, corresponding to a CO_2 laser.

The drawback of the phase plate is that it now acts as a high-pass filter, preventing the detection of wave numbers for which the distance from the optical axis $|\delta x|$ is smaller than the width of the groove. This is in fact a fundamental limit of the technique, as the lack of an external reference precludes the measurement of absolute phase changes: only phase *differences* across the width of the beam can be measured. The longest perpendicular *wavelength* that can be resolved is then of the order of the beam diameter, $\delta x = Fk/k_0 > \lambda_0 F/a$ which implies that $|k| > 2\pi/a$.

In practice, the maximum *wave number* that can be resolved unambiguously is set by the Nyquist condition on the spatial sampling, i.e., by the number of detector elements and their spacing in the object plane. For a given beam width and detector dimension, spatial resolution can be increased by enhancing the magnification through a set of lenses placed before the detector, and projecting only a fraction of the beam onto the detector. The cost is, however, a reduced field of view and a reduced diameter of the cylindrical interaction volume in the plasma.

Because of the line integration, the measured intensity modulation will be a sum of all fluctuating components along the beam path. In this setup PCI will therefore not have any longitudinal localisation (i.e localisation along the laser beam path). However, by using the anisotropy of turbulent structures in magnetically confined fusion plasmas along with the twist of the magnetic field, longitudinal localisation can in fact be achieved, as discussed next.

A. Longitudinal localisation

Fluctuations with sufficiently large wave number in the direction of beam propagation are averaged out upon integration. It follows that the measured intensity modulation is mainly sensitive to wave vectors perpendicular to the beam, i.e $k \sim k_{\perp,0}$. Furthermore, the turbulent structures are elongated along the field lines and the wave vector of the turbulent fluctuations is predominantly perpendicular to the magnetic field, $k_{\perp,B} \gg k_\parallel$. The wave vector detected by the PCI diagnostic, k_{meas}, is therefore due to fluctuation contributions that are mainly perpendicular to both the beam propagation direction and the total magnetic field, i.e., $k_{\text{meas}} \parallel B \times k_0$. Since the magnetic field in the fusion device twists, k_{meas} will rotate by an angle that is a function of the coordinate ℓ along the beam path[4], as is indicated in Fig. 2.

The scattered components of the beam in the focal plane and the propagation direction in the image plane will rotate accordingly. By placing a narrow angular filter in a focal plane, measurements will be limited only to wave vectors that fall inside this range, which in turn corresponds to a specific segment of the full beam path in the plasma. The integration is then effectively performed over a reduced length, yielding some degree of spatial localisation. The minimum angle range that can be selected is again limited by diffraction.

The technique considered in this work for localising the measurement involves a one-dimensional detector array combined with a rotatable filter. However, it should be noted that localisation can also be achieved without using an angular filter, by employing a two-dimensional detector instead. In this case the selection of the measured wave vector can be done numerically through a Fourier decomposition of the wave numbers, and then applying the selection rule $k_{\text{meas}} \parallel B \times k_0$[18,20]. While this two-dimensional technique gives a complete profile of the fluctuations for each time instant, a one-dimensional detector array combined with a rotatable filter usually provides a higher wave-number resolution and dynamic range.

B. The equation for the measured fluctuating intensity

In this work we consider a stigmatic C02 laser beam with a wave length 10.6 μm and thus a frequency $\omega = 28.3$THz which is much larger than the electron plasma frequency ω_p and the electron gyro frequency ω_c in typical fusion devices, such as TCV and JT-60SA. For example, in TCV $\omega_p \leq 90$ GHz and $\omega_c \sim 40$ GHz. The wave length is also shorter than the typical size of the fluctuations, ~ 5 mm. The conditions for the PCI system are therefore well satisfied, and the only effect of the plasma on the laser beam is a phase shift, as described above. Furthermore for a typical length of the interaction volume, ~ 1 m, diffraction within the interaction volume is negligible, and the laser beam rays deviates less than 10 μm from a straight line. We approximate the incident laser beam field with a stigmatic Gaussian beam, whose transverse width is described by the following equation

$$E_{p0}(r,p) = \left(\frac{8\pi}{c}P\right)^{1/2}\left(\frac{2}{\pi}\right)\frac{1}{w_0}e^{-\left(\frac{r^2+p^2}{w_0^2}\right)}, \qquad (5)$$

where P is the total beam power, and w_0 is the $1/e$ half-width of the laser beam. The Gaussian field is truncated by the pupil function P_a

$$P_a(r,p) = \begin{cases} 1, & \text{if } \sqrt{r^2+p^2} \leq a \\ 0, & \text{otherwise}, \end{cases} \qquad (6)$$

representing the effect of the aperture that is the most restrictive optical component limiting the perpendicular size of the laser beam to the diameter, $2a$, of the aperture. The coordinates r and p represent the Cartesian space perpendicular to the laser beam propagation direction, k_0, and are introduced in Fig. 3.

After scattering, the laser beam field is focused onto the focal plane where a phase plate is used to create the phase contrast between scattered and unscattered components. A spatial filter is also used for longitudinal localisation of the PCI signal and to select the measured wave-vector direction. The action of the phase plate and the spatial filter can be described with the transfer function T that acts on the scattered laser beam field $P_a E_{p0}(1+\delta\varphi)$ through the circular convolution operator $\circ$: $\left[T \circ \left(P_a E_{p0}(1+\delta\varphi)\right)\right](r,p)$. To first order in the fluctuating phase, $\delta\varphi$, the measured fluctuating intensity can then be
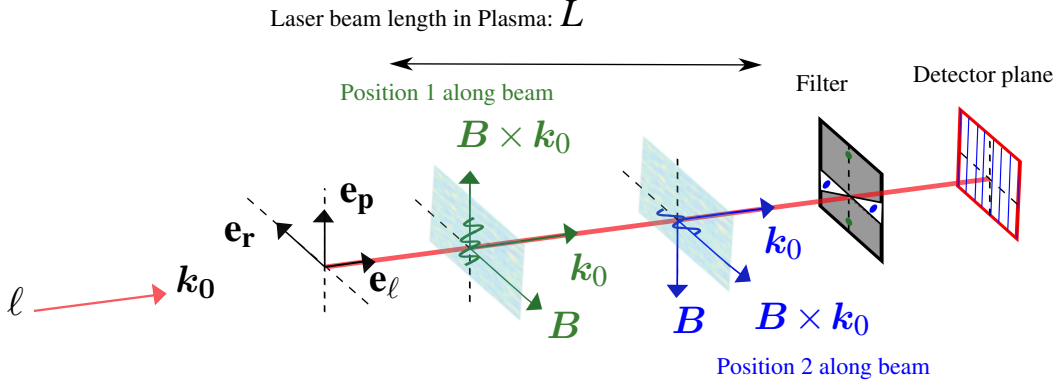
FIG. 2. Principle of the magnetic field curvature technique to achieve longitudinally localised measurements.
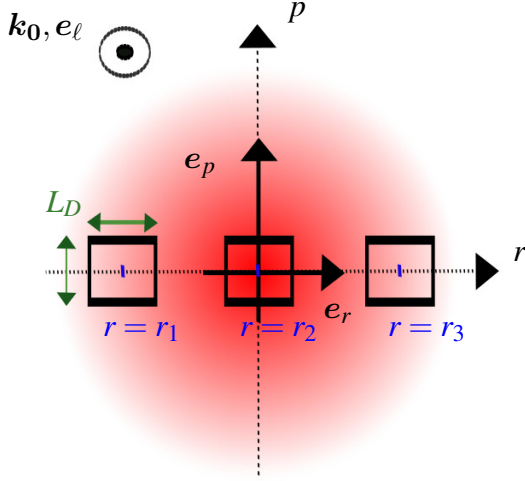

FIG. 3. Cartesian coordinate system composed of the vectors e_r, e_p perpendicular to the beam and e_ℓ aligned with the PCI laser beam propagation direction k_0. A detector element i occupies a subvolume that is centered at $r = r_i, p = 0$. In this case we show three detector elements, thus $i = 1, 2, 3$. The detector elements are square with side L_D.

written as[1]

$$\tilde{\mathscr{E}}(Mr, Mp, t) = \frac{c}{4\pi M^2} \mathrm{Im} \left\{ \left[T \circ (P_a E_{p0}) \right] (r, p) \times \right.$$
$$\left. \left[T \circ (P_a E_{p0} \delta\varphi) \right]^* (r, p, t - t_d) \right\} =$$
$$\frac{c}{4\pi M^2} r_e \lambda_0 \int_L \mathrm{d}\ell \, \mathrm{Im} \left\{ \left[T \circ (P_a E_{p0}) \right] (r, p) \times \right.$$
$$\left. \left[T \circ (P_a E_{p0} \delta n_e) \right]^* (r, p, t - t_d) \right\} \quad (7)$$

where we made use of Eq. (1). The intensity is evaluated at the coordinates (Mr, Mp) in the detector plane that corresponds to the coordinates (r, p) in the object plane. Here M is the aggregate magnification of the optical set-up. The time delay t_d in Eq. (7), between the scattering event and the measurement in the detection plane, can for the parameters we consider be treated as a constant and will therefore henceforth be omitted.

The synthetic diagnostic implements Eq. (7), as will be described in the next section.

III. THE SYNTHETIC PCI DIAGNOSTIC

In this section, we will present the details of the synthetic diagnostic that models the experimental PCI measurements. The first step, presented in subsection III A, is to generate electron density fluctuations with gyrokinetic simulations. In the following examples we will take simulations from the GENE code, but the synthetic diagnostic can easily be adapted to other gyrokinetic codes by appropriately modifying the mapping of the coordinates between the simulation and the diagnostic volumes. In subsection III B we show how we post-process these fluctuations to obtain the unfiltered PCI signals, including how we implement the spatial filtering in the synthetic diagnostic.

Throughout this paper we illustrate the synthetic PCI diagnostic by modelling measurements from the PCI system installed on the TCV tokamak, where the laser beam is sent nearly tangentially through the plasma. The path of the laser beam through the plasma, projected on a poloidal cross-section and subdivided into a set of detector chords, is shown in Fig. 4. An illustration of the toroidal propagation in TCV is shown in Fig. 5. In this example the PCI beam covers a radial coordinate going from edge to midradius, as shown in Fig. 6. In subsection IV we will see however that the spatial filtering can reduce the contributions to the PCI signals down to a small segment near midradius, as indicated with the green lines in Fig. 4. The tangential configuration leads to a fast rotation of the measured wave-vector, and consequently very good localisation. This will be confirmed from first principles in subsection IV.

A. Generating δn_e

Electron density fluctuations δn_e are generated with the Eulerian (grid-based) local (flux-tube) version of the GENE[7,21] code, which enables one to carry out kinetic simulations of plasma turbulence by numerically solving the gyrokinetic equation for evolving the species distributions in phase space. The local approximation implies that no radial variation of profiles and their gradients as well as magnetic geometric coefficients are taken into account; rather, fluctuations are
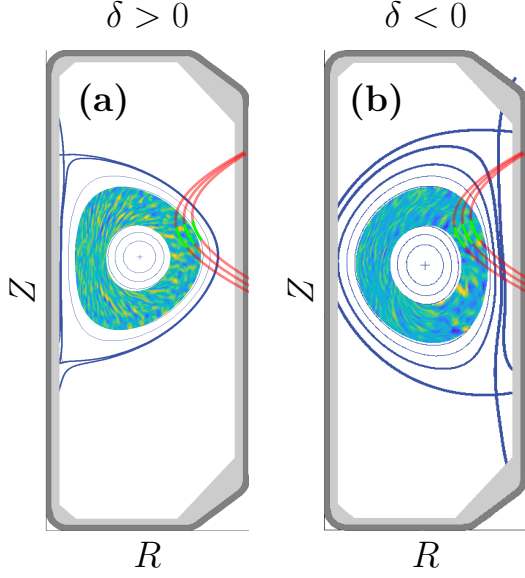
FIG. 4. PCI set-up in TCV: laser beam (red) divided into several rays on top of a snapshot (in the poloidal plane in a flux tube centered around the tangency point) of electron density fluctuations generated by GENE. The light green segments illustrate the reduced, localised segments that can be selected with the spatial filters. In the actual set-up used until now there are 9 non-equidistant rays corresponding to 9 non-equidistant detector elements.
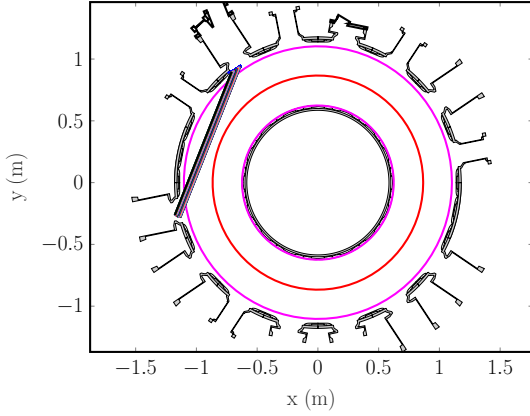

FIG. 5. The tangential beam geometry of the PCI system shown on a toroidal cross-section of TCV. The position of the innermost and outermost flux surfaces is shown in purple while the magnetic axis is shown in red.

generated based on input parameters that apply to one radial position, where the normalised radial variable is typically chosen as given by ρ_t, the square root of the normalised toroidal flux. Electron density fluctuations $\delta n_e = \delta n_e(x, y, z)$ provided by the GENE simulations are represented in field-aligned coordinates x, y, z where x is the radial and y the binormal coordinate, while z is the straight-field-line poloidal angle parametrising the position along a given field line (note that $\boldsymbol{B} \parallel \nabla x \times \nabla y$ so that $x = $ const and $y = $ const defines a
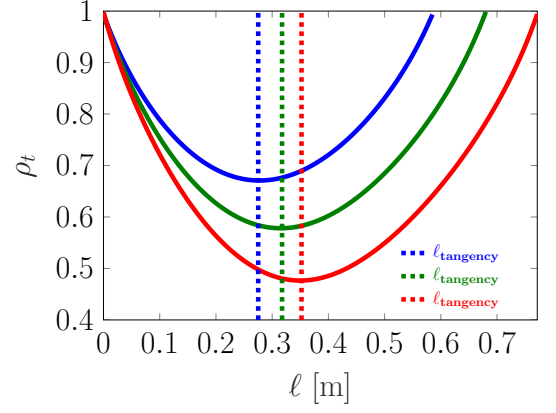

FIG. 6. Radial ρ_t coordinate as a function of beam propagation length ℓ for three PCI rays, for a positive triangularity equilibria (discharge 49052). The position $\ell = \ell_{\text{tangency}}$ denotes the tangency point and coincides with the point along the ray where $\partial \rho_t / \partial \ell = 0$. For purely radial modes, $k_y = 0$, it is equal to the position $\ell_\perp$, introduced in Eq. (19), where the wave vector is perpendicular to the laser beam propagation direction $\boldsymbol{k}_0$. Each ray is distinguished by the r coordinate introduced in subsection III B, with $r = r_1$ (blue ray), $r = r_2$ (green ray) and $r = r_3$ (red ray).

magnetic line). The curvilinear coordinate system (x, y, z) is clearly non-orthogonal. The coordinates' expressions in terms of the radial position ρ_t, the toroidal angle ϕ and the straight-field line poloidal angle χ are given by

$$
\begin{aligned}
x &= \rho_t - \rho_{t,0}, \\
y &= C_y \left[q(\rho_t)\chi - \phi \right], \\
z &= \chi,
\end{aligned}
\tag{8}
$$

where q is the safety factor, $C_y = r_0/q_0$, $q_0 = q(r_0)$ and $r_0 = a\rho_{t,0}$ is the radial position of the centre of the flux tube with a being the minor radius. Periodicity is assumed in the radial and binormal directions, so that fluctuations are conveniently represented in Fourier space along x and y with associated wave numbers k_x and k_y respectively. A linearised safety factor profile, $q(x) = q_0 \left[1 + \hat{s}(x - \Delta x)/r_0 \right]$ with a shift Δx, is considered in Eq. (8). The shift Δx ensures continuity in the parallel coordinate z when crossing the inner midplane, see Appendix A. Toroidal symmetry is reflected in (x, y, z) coordinates by invariance with respect to y. Linear eigenmodes thus have fixed k_y related to toroidal mode number n by the relation: $k_y = nq_0/r_0$. Since microinstabilities are field-aligned with $nq_0 \approx m$, where m is the poloidal mode number, $k_y \approx m/r_0$ is an estimate of the poloidal wave number. With respect to $z \in [-\pi, \pi)$, fluctuations are however represented in direct space considering a finite difference scheme based on mesh $\{z_{j=0,...,n_z-1}\}$. Note that k_y might not necessarily correspond to an integer toroidal mode number n if the flux tube does not cover an integer division of the toroidal angle. However, in this paper, for properly mapping the flux tube onto the synthetic volumes in the synthetic diagnostic, in all simulations L_y was chosen such that k_y translates to an integer toroidal mode number n.

In this paper we generate electron density fluctuations for a positive and a negative triangularity TCV discharge. For a proper modelling of a TCV scenario it is necessary to consider three kinetic species in our simulations: main deuterium ions, electrons and carbon impurities. Furthermore, collisions also have to be retained, here modelled with the linearised Landau collision operator, while electromagnetic effects can be neglected for these TCV-relevant simulations where $\beta_e \sim 0.1\%$. Finally, we consider also an experimental magnetic geometry provided with the MHD code CHEASE[22].

Density and temperature profiles for the positive triangularity scenario #49052 ($\delta_{\text{LCFS}} = 0.5$) and negative triangularity scenario #49051 ($\delta_{\text{LCFS}} = -0.25$), both with an equal amount of 460 kW central ECH power, are shown in Fig. 7. Here δ_{LCFS} stands for the triangularity at the Last Closed Flux Surface (LCFS). These profiles have been generated by using a Kinetic Equilibrium Reconstruction (KER)[23]. The aim of KER is to identify the plasma state given available measurements of profiles and/or first principle modelling. This is achieved by iterating over pressure profiles combined with a calculation of the deposited heat and current drive, and a reconstruction of the plasma equilibrium. The computation is run until convergence when all results match the available constraints in a least-squares sense. As input to KER we provide the electron pressure measured by the Thomson scattering diagnostic, while the ion density is estimated from quasineutrality and the ion temperature is estimated using the PRE-TOR formula.

We center the flux tube in the GENE simulations at $\rho_{t,0} = 0.6$, corresponding to the magnetic surface to which the central ray $r = r_2$ is tangent, as seen in Fig. 6. Parameters at this radial position for the two discharges are shown in Table I. There, $\beta_e = 8\pi n_e T_e / B_0^2$ is the normalised plasma kinetic to magnetic pressure, $r_a/L_{T,n}$ is the normalised gradient length scale, $Z_{\text{eff}} = (n_i + 36n_C)/n_e$ is the effective charge and $\nu_c = \pi \ln\Lambda e^4 n_e r_a /(2^3/2T_e^2)$ is a normalised collision frequency used in GENE, where $\ln\Lambda$ is the Coulomb logarithm. The input parameters differ between the two scenarios as a consequence of the equal ECH heating but different transport properties. The experimental heat flux values are $Q_e = 658 \pm 70$ kW, $Q_i = 10 \pm 5$ kW for $\delta > 0$ and $Q_e = 616 \pm 70$ kW, $Q_i = 11 \pm 5$ kW for $\delta < 0$. Since for $\delta < 0$ the electron heat flux is similar to $\delta > 0$, but the electron temperature is larger, it suggests that TEMs are weaker. The stabilisation of TEMs could be due to the increased collisionality and dilution in the $\delta < 0$ case due to increased impurity density. This in turns leads to a more peaked T_e profile and thus an increased electron temperature gradient. Another explanation for the similar heat fluxes but different parameters could also be a stabilisation of ITG turbulence, also due to impurities. The contribution of ITG to Q_e would then also be lower.

For the non-linear GENE simulations we consider the grid $N_x \times N_y \times N_z \times N_{v_\parallel} \times N_\mu \times N_s = 256 \times 64 \times 48 \times 30 \times 16 \times 3$, where the resolutions refer to the number of discretization points along the three spatial directions (x,y,z), the two velocity space directions $(v_\parallel, \mu)$, and the number of particle species s respectively. The radial and binormal simulation box sizes
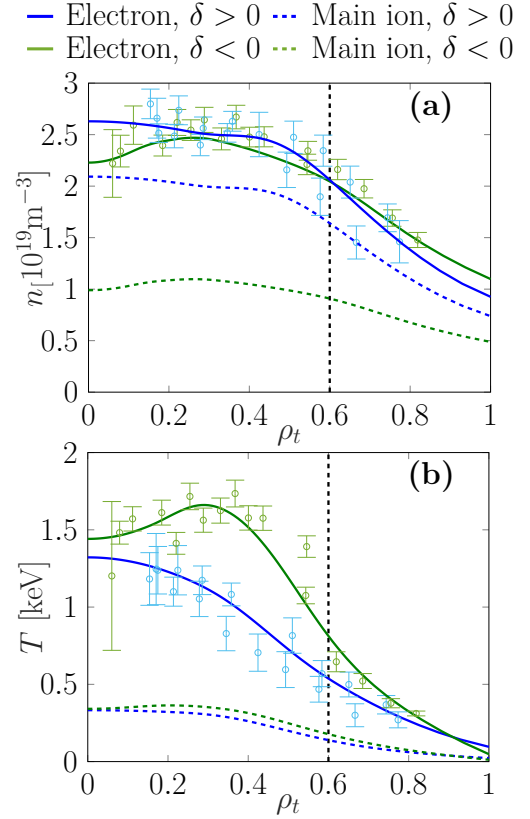

FIG. 7. Density (a) and temperature (b) profiles for electrons (solid lines) and ions (dashed lines) for positive (blue) and negative (green) triangularity cases.

TABLE I. Parameters of the positive triangularity shot #49052 and negative triangularity shot #49051 (blue font and in parentheses) at $\rho_t = 0.6$ used as input to the GENE simulations, obtained from the MHD equilibrium code CHEASE[22] and species profiles shown in Fig. 7. The reference magnetic field is provided at the magnetic axis. The parameter r_a is the minor radius and R is the major radius. In bold we show important parameters undergoing a large change when changing from positive to negative triangularity.

n_e [10^{19}m^{-3}]	2.10 (2.12)	T_i/T_e	0.26 (0.22)
q_0	**1.47 (1.21)**	T_e [keV]	0.54 (0.88)
$r_a/L_{n,e}$	1.48 (1.14)	$\hat{s}$	**1.44 (1.22)**
B_0 [T]	1.55 (1.50)	$r_a/L_{n,i}$	1.48 (1.14)
R/a	3.12 (3.17)	r_a [m]	0.27 (0.28)
$r_a/L_{T,e}$	**2.81 (3.62)**	β_e [10^{-3}]	0.18 (0.34)
n_i/n_e	**0.76 (0.36)**	$r_a/L_{T,i}$	3.75 (3.42)
ν_c [10^{-3}]	**0.78 (0.27)**	Z_{eff}	**2.2 (4.2)**

are different for the two scenarios, with $L_x = 128\,\rho_i$, $L_y = 112$ ρ_i for $\delta > 0$ (ρ_i is the ion Larmor radius), and $L_x = 142\,\rho_i$, $L_y = 152\,\rho_i$ for $\delta < 0$ as a consequence of the different values of $\hat{s}$ and q_0. For the same number of radial and binormal wave numbers we therefore have $\max(k_y\rho_i) = 3.54$, $\max(k_x\rho_i) = 6.24$ for $\delta > 0$ and $\max(k_y\rho_i) = 2.6$, $\max(k_x\rho_i) = 5.6$ for $\delta < 0$.

Adaptive hyperdiffusivities[24] in x and y are used to simulate damping provided otherwise by small-scale modes that are not included in this simulation. All non-linear simulations are performed for a sufficiently long time, $t_{sim} > 900\ a/c_s$ where $c_s = \sqrt{T_e/m_i}$ is the sound speed, to generate enough statistics of the density fluctuations.

For the considered parameters, we find the simulated ion and electron heat flux $Q_e = 152$ kW, $Q_i = 10$ kW for $\delta > 0$ and $Q_e = 504$ kW, $Q_i = 3$ kW for $\delta < 0$. In both cases, but especially for $\delta > 0$, we see that GK simulations that used KER to generate input profiles underestimate the experimental heat flux values. We can better understand the change in the heat fluxes by looking also at linear GENE simulations, and compute the growth rate γ and frequency ω of the most unstable mode, as shown in Fig. 8. For $\delta > 0$ we see TEMs ($\omega < 0$) at large scales ($k_y\rho_i < 0.6$) and ITG modes ($\omega > 0$) at smaller scales ($k_y\rho_i > 0.6$). For now we focus on the modes for $k_y\rho_i \leq 2$. If we keep the parameters (such as gradients and densities) of the $\delta > 0$ case but using the equilibrium of $\delta < 0$ we clearly stabilise both ITG and TEMs at these scales. Adding also the actual parameters of $\delta < 0$ leads to a slight increase of the TEM growth rates, due to the larger T_e and $r_a/L_{T,e}$. The orange line shows the stabilisation due to the increased impurity content in $\delta < 0$. For this case we kept all the parameters of $\delta > 0$, including the equilibrium, but then took the carbon impurity density n_c from the $\delta < 0$ (adjusting n_i for quasineutrality) case. This clearly stabilises both TEM and ITG modes. Finally, we yet again illustrate the stabilising role of triangularity by changing the equilibrium to $\delta > 0$ but keeping the parameters of $\delta < 0$ case, showing an increase in the growth rates.

In view of these observations we can interpret the change of the non-linearly simulated ion heat flux going from $\delta > 0$ to $\delta < 0$. The reduction in the heat flux is due to a stabilisation of ITG modes at the considered scales, which is a combined effect of an increased impurity content and the change in the plasma shape. Q_i underestimates the experimental value for the $\delta < 0$ case, since the ITG suppression due to carbon is most likely overestimated for this case. An increased electron temperature gradient is observed for the $\delta < 0$ case, where TEMs are stabilised by increased collisionality and the negative triangularity. Better agreement with experiments could be achieved by varying input parameters within experimental error bars. This was not done in the present work where the aim of the simulations was to make a first test of the synthetic diagnostic, rather than exactly reproducing the experimental heat flux levels.

Finally, in Fig. 8 we note that at smaller scales, above $k_y\rho_i > 2$ the effect of changing from $\delta > 0$ to $\delta < 0$ is very different, in fact the growth rates have increased substantially. Even though this mode is propagating in the ion diamagnetic
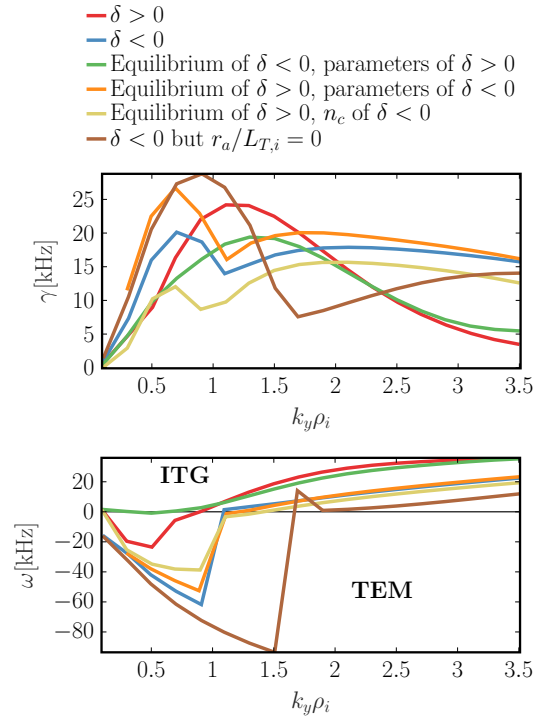

FIG. 8. Linear simulations illustrating the growth rate (top) and frequency (bottom) for the $\delta > 0$ case (red) and $\delta < 0$ case (blue). We also show the result (green) we obtain when we take the equilibrium from $\delta < 0$ but take the parameters (gradients, temperatures and densities) from $\delta > 0$. The opposite is shown in orange. Finally, we show what we obtain when we take the case of $\delta > 0$ but the Carbon impurity density n_c from $\delta < 0$ (yellow) and also the case of $\delta < 0$ but with the ion temperature gradient set to 0 (brown).

direction ($\omega > 0$) this appears to be an instability of different nature than the ITG mode seen for $k_y\rho_i \leq 2$, as it appears even if the ion temperature gradient $r_a/L_{T,i}$ is set to 0. We did not investigate further the nature of this mode, as in the non-linear simulations it has little effect given that the heat fluxes usually peak around γ/k_y. We confirm this in Fig. 9 where it is clearly seen that the main contribution to the density fluctuations, apart from the zonal flow $k_y = 0$ component, is for $k_y\rho_i < 1$ while for larger scales there is a cascade in k_y of decreasing fluctuation amplitude.

Electron density fluctuations obtained from non-linear GENE simulations are post-processed with a synthetic diagnostic to model measurements from TPCI as discussed in the next section.

B. Generating the synthetic signals

The synthetic diagnostic aims to model the intensity of the electron density fluctuations measured by the square-law detectors. As described in Section II, the measured fluctuating intensity originates from an incident laser beam field that is scattered by the electron density fluctuations, and the mea-
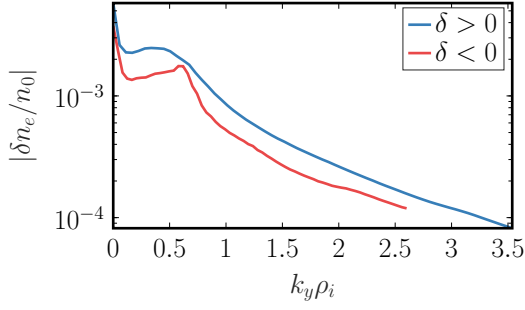
FIG. 9. k_y spectra, averaged over all k_x and z, of the electron density fluctuations simulated with non-linear GENE simulates. In blue is the $\delta > 0$ case while in red is the case with $\delta < 0$.

sured fluctuating intensity is given by Eq. (7).

We implement Eq. (7) in subsection III B 1 taking into account a finite aperture, $P_a(r,p)$, and a Gaussian distribution of the incident laser field, $E_{p0}(r,p)$. While this gives the most proper estimate of the PCI signals, in this approach it is difficult to see the contribution from individual GENE k_x and k_y modes to the PCI signals. It is more insightful to write the synthetic signals directly in terms of their GENE k_x and k_y contributions, as presented in subsection III B 2. To make it computationally efficient, in this approach we simplify, by assuming the aperture a to be infinite and describing the incident laser beam as a plane wave. Further simplifications are made thanks to the separation of scales, with the beam diameter ($2w_0 \geq 5$ cm) being larger than the size of a typical turbulence eddy (~ 5 mm) which in turn is larger compared to the size of the detector elements (~ 0.25 mm). As will be shown in the end of subsection III B 2, these simplifications do not alter the main signatures of the synthetic signal, yet the approach reveals useful information on the role of different k_x and k_y modes.

1. Gaussian beam and finite aperture

We consider the proper case first, and describe the laser beam E_{p0} with a Gaussian function as described by Eq. (5), truncated by the pupil function in Eq. (6).

From the gyrokinetic GENE simulations we have obtained the electron density fluctuations $\delta n_e(x,y,z)$ inside a flux tube, centred around the radial position $\rho_0 = 0.6$, the laser beam being tangent to the corresponding magnetic surface. These density fluctuations have to be interpolated onto a coordinate system aligned with the PCI laser beam before we can conveniently compute the measured intensity in the detector plane.

To compute the synthetic PCI signal we represent the laser beam in the Cartesian coordinate system e_r, e_p, e_ℓ where ℓ is the coordinate along the beam direction while r, p represent the two coordinates perpendicular to the beam, as shown in Fig. 3.

From the equilibrium generated by CHEASE, we may transform the detector coordinates r, p, ℓ to the magnetic coordinates $\chi(r,p,\ell), \phi(r,p,\ell), \rho_t(r,p,\ell)$ as well as compute the safety factor, $q(r,p,\ell)$ which then through Eq. (8) can be transformed to the field-aligned GENE coordinates $x(r,p,\ell), y(r,p,\ell), z(r,p,\ell)$. We then interpolate the electron density fluctuations generated by GENE to obtain the fluctuations $\delta n_e(x(r,p,\ell), y(r,p,\ell), z(r,p,\ell))$ within the laser beam.

The next step is to apply the effect of the phase plate to obtain the phase contrast between scattered and unscattered components. As discussed in Section II, the phase plate is placed in the focal plane where it introduces a 90° phase change to components of the laser beam passing through a central groove. In Fourier k_r, k_p space the phase plate can be described with the function

$$\hat{T}_G = 1 + P_{k_c}(k_r, k_p) \left(i\sqrt{\rho} - 1 \right), \tag{9}$$

where the pupil function P_{k_c} is given by Eq. (6) and $\rho \leq 1$ is the power transmissivity that enhances the contrast by attenuating the unscattered component of the beam. The hat is used to indicate that we now consider the Fourier transform of the real space transfer function T appearing in Eq. (7). The cut-off wave number, $k_c = k_0 v/F$, is related to the half-width of the groove, v, which is of the order of the diffraction half-spot of the unscattered component. The role of $\hat{T}_G$ for calculating the intensity in Eq. (7) can be understood with the help of the Fourier-transforming property of lenses. A lens placed after the object is used to focus scattered and unscattered components of the laser beam onto the phase plate. The unscattered component is given by the term $P_a E_{p0}$ in Eq. (7) whose field distribution in the focal plane is proportional to $\mathscr{F}\left[P_a E_{p0} \right](k_r, k_p)$, where $\mathscr{F}[\cdot](k_r, k_p)$ denotes the spatial Fourier transform. Correspondingly, the distribution in the focal plane of the scattered part of the beam, which is affected by the electron density fluctuations, is proportional to $\mathscr{F}\left[P_a E_{p0} \delta n_e \right](k_r, k_p)$. The effect of the phase plate can thus be written as a simple multiplication of both scattered and unscattered components with $\hat{T}_G$. In real space this operation is represented as a convolution, as written in Eq. (7).

We demonstrate the effect of the phase plate on an artificial density fluctuation composed of three fluctuating components, $\delta n_e(r,p) = 10\cos(0.25k_c p) + \cos(10k_c p) + \cos(5k_c r)$ as illustrated in the leftmost plot in Fig. 10. When applying $\hat{T}_G$ the part of the density fluctuation with $k < k_c$ that scatters the laser beam into the groove, is filtered out, while the remaining components lead to a measurable intensity, as shown in the central plot in Fig. 10. The reduction of the fluctuation amplitude towards the borders is a consequence of the Gaussian form of the incident laser beam, while the circular cut is due to the Pupil function P_a

Given the actual density fluctuations generated by GENE, $\delta n_e(x(r,p,\ell), y(r,p,\ell), z(r,p,\ell))$, the scattered and unscattered field distributions are calculated using the Fourier transform, before applying Eq. (9), transforming back to real space and finally evaluating the intensity through Eq. (7).

In addition to the phase plate, in this paper we include the effect of a spatial filter that is also placed in the focal plane. As discussed in section II such a spatial filter can be used to restrict the wave vectors that contribute to the PCI signals. If we assume that the measured wave vector satisfies $k \parallel k_0 \times \mathbf{B}$ and this direction varies along the laser beam, each wave vec-

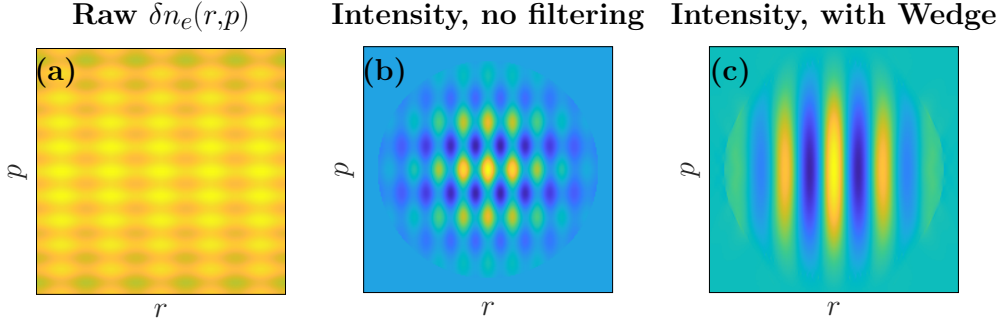Raw $\delta n_e(r,p)$ Intensity, no filtering   Intensity, with Wedge

FIG. 10. An artificial electron density fluctuation composed of three fluctuation components (a), the corresponding intensity calculated with Eq. (7) when applying the effect of a phase plate (b) and the intensity when also including a wedge filter (c). The filters are represented in wave-number space (k_r, k_p) but could equally be represented in real space (r, p), where they would have the same shape.

tor direction translates to a specific position ℓ along the beam. The spatial filter therefore selects both which wave vector directions contribute to the PCI signal, and where in the plasma the signal is coming from. Our goal now is to derive the selection rules naturally by performing the line integration directly, i.e., by implementing a truly faithful synthetic diagnostic.

We will consider two different spatial filtering configurations, the wedge and the straight filter, which are alternately used in the PCI set-up. Similarly to the phase plate, the action of the spatial filter is included through a multiplication of the field distribution of unscattered and scattered components in Fourier space, with a mask function. In the case of a straight filter only the part of the focal spot falling inside the width $\pm k_S$, of the filter contributes to the PCI signals. Thus k_S is the upper cut-off wave number in this filter configuration. The straight filter can in Fourier space be represented with the mask function

$$\hat{T}_S(k_r, k_p) = \begin{cases} 1, & \text{if } |k_p| \leq k_S \\ 0, & \text{otherwise.} \end{cases} \tag{10}$$

An example of the straight filter is shown on the right-hand side of Fig. 11. Optimal localisation is achieved when k_S is minimum, and thus equal to k_c. Since the measured wave-vector rotates along the laser beam path, the straight filter configuration thus leads to an optimal localisation for each wave number $|\boldsymbol{k}_{\perp,0}|$. Fluctuations with larger $|\boldsymbol{k}_{\perp,0}|$ fall more quickly outside the filter domain and are therefore more localised. The filter therefore leads to a non-uniform localisation of the fluctuation contributions.

The wedge filter configuration instead provides a uniform localisation by including any contribution falling inside a wedge, with a wedge half angle θ_W. In this case the mask function is given by

$$\hat{T}_W(k_r, k_p) = \begin{cases} 1, & \text{if } \left| k_r / \sqrt{k_r^2 + k_p^2} \right| \geq \cos\theta_W \\ 0, & \text{otherwise.} \end{cases} \tag{11}$$

Similarly as for the straight filter configuration, the smallest wedge half angle is limited by diffraction. From the illustration of the wedge filter in Fig. 11 we see that a given $|\boldsymbol{k}_{\perp,0}|$
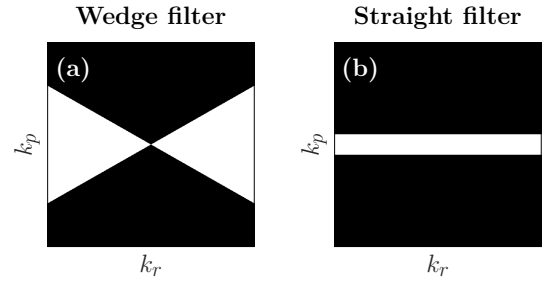
Wedge filter   Straight filter

FIG. 11. The wedge (left) and straight (right) configurations used for spatial filtering in the PCI set-up. Fluctuations that scatter the laser light onto the filter domain (white colors) contributes to the PCI signals while other components are strongly damped (black).

stays within the filter over a larger angle and thus over a larger portion of the laser beam. The wedge filter thus provides uniform localisation for each $|\boldsymbol{k}_{\perp,0}|$ that falls inside the filter. In this fashion, this filtering choice retains the strict imaging properties of the technique. In this case the localisation will be limited by the smallest $|\boldsymbol{k}_{\perp,0}|$ that is included in the measurement, and thus this leads to a worse localisation compared to the straight filter case that optimises the integration length for each $|\boldsymbol{k}_{\perp,0}|$.

Notice that the straight and wedge filters in Fig. 11 are represented in wave-number space (k_r, k_p). They could equally well be represented in real space r, p on a focal plane, where they would have the same shape.

Both filter configurations are aligned along $\boldsymbol{e}_r$, meaning that any rotation of the filter necessarily involves a corresponding rotation of the image and consequently, the detector elements. The direction of $\boldsymbol{e}_r$ can thus be used to select the preferential (k_x, k_y) components. Normally we choose $\boldsymbol{e}_r \parallel \nabla x(\ell = \ell_{\text{tangency}})$ where ℓ_{tangency} is the position along the laser beam where it is tangent to the magnetic surface, which corresponds to the point in Fig. 6 where the derivative $d\rho_t / d\ell$ goes to zero. The effect of the spatial filter, in this case the wedge filter, is illustrated in the rightmost plot in Fig. 10. It filters out the high k component of the artificial density fluctu-

ation, propagating purely in the e_p direction. After applying both the phase plate groove and the spatial filter the remaining part of the artificial density fluctuation is the component $\cos(5k_c r)$ that scatters the laser beam both outside the phase plate groove, and within the spatial filter.

The total effect of the phase plate and spatial filters is thus given by a multiplication of scattered and unscattered field distributions in the focal plane with the total transfer function. In the case of the straight filter configuration it is $\hat{T} = \hat{T}_G \hat{T}_S$ and $\hat{T} = \hat{T}_G \hat{T}_W$ in the case of the wedge filter configuration.

Finally, to obtain the synthetic PCI signals we have to average over the detector area. The synthetic signal for a given detector element, i centred at $r = r_i$ and $p = 0$ (as illustrated in Fig. 3)) is given by

$$\langle I \rangle (r_i, t) = \int_{-L_D/2+r_i}^{L_D/2+r_i} \int_{-L_D/2}^{L_D/2} dr\,dp\,\tilde{\mathscr{E}}(Mr, Mp, t), \quad (12)$$

where L_D is the square length of the detector elements as is illustrated in n Fig. 3.

2. Synthetic PCI signal in terms of GENE k_x and k_y modes

The procedure described in the previous subsection gives the most proper estimate of the PCI signals. However, starting from the point when we computed the electron density fluctuations on the Cartesian grid, $\delta n_e(r, p, \ell, t)$, we lost track of how the different k_x and k_y GENE fluctuation components individually contribute to the PCI signals. Of course, it is possible to retrieve this information by artificially modifying the input GENE fluctuations when calculating Eq. (7) (for example by removing all but one k_x, k_y component, and then repeating the procedure for all k_x and k_y values), however it is more convenient and insightful to directly write the synthetic signal in terms of the GENE k_x and k_y modes.

To make this computationally efficient, we make several simplifications. First, instead of a Gaussian we assume the incident beam to be an infinite plane wave, and thus equal to a constant, $E_{p0}(r, p) = E_{p0}$. The aperture is also assumed to be infinite. In this case the measured intensity in Eq. (7) can be rewritten as[1]

$$\tilde{\mathscr{E}}(Mr, Mp, t) = \frac{\sqrt{\rho}c E_{p0}^2}{4\pi M^2} r_e \lambda_0 \int_L d\ell\,[T \circ \delta n_e](r, p, t), \quad (13)$$

where the transfer function T here is slightly different from T appearing in Eq. (7).

Consider then the electron density fluctuations represented as a Fourier sum with respect to time and summed over the radial k_x and binormal k_y GENE components

$$\delta n_e(r, p, \ell, t) = \sum_{k_x}\sum_{k_y} \delta n_e(t, k_x, k_y, z(r, p, \ell), t)$$
$$\times e^{ik_x x(r,p,\ell)+ik_y y(r,p,\ell)}, \quad (14)$$

such that the intensity, Eq. (13), averaged over each detector

element i is given by

$$\langle I \rangle (r_i, t) = \frac{\sqrt{\rho}c E_{p0}^2}{4\pi M^2} r_e \lambda_0 \int_L d\ell \int_{-L_D/2+r_i}^{L_D/2+r_i} \int_{-L_D/2}^{L_D/2} dr\,dp$$
$$\times \sum_{k_x}\sum_{k_y} \hat{G}(k_r(k_x, k_y, r, p, \ell), k_p(k_x, k_y, r, p, \ell))$$
$$\times \delta n_e(k_x, k_y, z(r, p, \ell), t) e^{ik_x x(r,p,\ell)+ik_y y(r,p,\ell)}. (15)$$

Here we have introduced the function $\hat{G}$ that is related to the Fourier transform of $T(r, p)$ appearing in Eq. (13) but contains the necessary terms to make the coordinate transformation from (r, p, ℓ) to (x, y, z), valid. In the following we will actually not explicitly compute $\hat{G}$ by defining $T(r, p)$. Instead we directly choose $\hat{G}$ such that it correctly captures the effect of the various filters on a given k_x and k_y mode.

To simplify further we assume that the Fourier amplitudes of the fluctuations are constant across the transverse width of the detectors, e.g $\delta n_e(k_x, k_y, z(r, p, l), t) \sim \delta n_e(k_x, k_y, z(r_i, 0, \ell), t) \equiv \delta n_e(k_x, k_y, z(r_i, \ell), t)$. Furthermore we expand the phase term such that $k_x x(r, p, \ell) + k_y y(r, p, \ell) \sim k_x x(r_i, 0, \ell) + k_y y(r_i, 0, \ell) + r k_r(r_i, 0, \ell, k_x, k_y) + p k_p(r_i, 0, \ell, k_x, k_y) \equiv k_x x(r_i, \ell) + k_y y(r_i, \ell) + r k_r(r_i, \ell, k_x, k_y) + p k_p(r_i, \ell, k_x, k_y)$, meaning that we regard the detector volumes as one dimensional rays. Both these simplifications are justified since the size of the detector elements (in the object plane, thus L_D is magnified by the magnification $1/M$) are very small compared to the typical size of a turbulence structure. In the end of this subsection we verify that indeed, after these simplifications, the synthetic signals retains the main signatures that are obtained in the proper case, subsection III B 1.

The wave numbers k_r and k_p appearing here are computed for each GENE wave number, k_x and k_y, and for every position along the laser beam. For a given k_x and k_y, the wave numbers k_r and k_p are computed using $k_r(r_i, \ell, k_x, k_y) = \boldsymbol{k}_{\perp,B}(r_i, \ell, k_x, k_y) \cdot \boldsymbol{e}_r$ and $k_p(r_i, \ell, k_x, k_y) = \boldsymbol{k}_{\perp,B}(r_i, \ell, k_x, k_y) \cdot \boldsymbol{e}_p$. The full wave vector is $\boldsymbol{k}_{\perp,B}(r_i, \ell, k_x, k_y) = k_x \nabla x(r_i, \ell) + k_y \nabla y(r_i, \ell)$ where the radial $\nabla x(r_i, \ell)$ and binormal $\nabla y(r_i, \ell)$ unit vectors for the GENE coordinates are evaluated at every position r_i, ℓ along the laser beam. The wave vector is then projected onto the unit vectors $\boldsymbol{e}_r$ and $\boldsymbol{e}_p$ in the r and p directions respectively. Unlike Eq. (12) the intensity in Eq. (15) thus only includes the wave numbers k_r and k_p that correspond to a mode k_x and k_y that actually exists in the GENE simulation. Henceforth, the dependence of k_r and k_p on k_x, k_y, r_i and ℓ is assumed, and therefore omitted in writing to simplify the notation.

Eq. (15) can thus be written as

$$\langle I \rangle (r_i, t) =$$
$$\frac{\sqrt{\rho}c E_{p0}^2}{4\pi} r_e \lambda_0 \int_L d\ell \sum_{k_x}\sum_{k_y} \hat{G}(k_r, k_p)\,\mathscr{T}_{av}(k_r, k_p)$$
$$\times \delta n_e(k_x, k_y, z(r_i, \ell), t) e^{ik_x x(r_i,\ell)+ik_y y(r_i,\ell)}, \quad (16)$$

where the function $\mathscr{T}_{av}(k_r, k_p)$ takes into account the effect of averaging the measured intensity over the detector area. It is derived from the integration of the intensity over the detector

area and is given by

$$\mathscr{T}_{\text{av}}(k_r, k_p) = \frac{4M^2}{L_D^2 k_r k_p} \sin\left(k_r \frac{L_D}{2M}\right) \sin\left(k_p \frac{L_D}{2M}\right). \quad (17)$$

Just as in the previous subsection, the transfer function $\hat{G}(k_r, k_p)$ contains the combined effect of the phase plate and spatial filters and is given by $\hat{G}(k_r, k_p) = \hat{G}_G \hat{G}_W$ for the wedge filter case and $\hat{G}(k_r, k_p) = \hat{G}_G \hat{G}_S$ for the straight filter case. The transfer function of the spatial filters, $\hat{G}_S$ and $\hat{G}_W$ are the same as T_S and T_W defined earlier, given by Eq. (11) and Eq. (10) respectively. The phase plate, however, is in this case described by the mask function, $\hat{G}_G$, given by

$$\hat{G}_G(k_r, k_p) = \begin{cases} 1, & \text{if } \sqrt{k_r^2 + k_p^2} \geq k_c \\ 0, & \text{otherwise.} \end{cases} \quad (18)$$

To verify the assumptions and approximations made in this subsection we compare the wave number spectrum calculated for the synthetic signals when considering the proper synthetic signals, computed using the approach in subsection III B 1, with the simplified approach described in this subsection. We consider δn_e generated for the positive and negative triangularity cases, using the parameters shown in Table I. The result, shown in Fig. 12, demonstrates that the simplified approach is able to reproduce the main trends of the synthetic signals: in particular, the asymmetry in the amplitudes of fluctuations propagating with $k_r > 0$ and $k_r < 0$, for both positive and negative triangularity cases. Henceforth we will rely on the results obtained using the simplified approach only, which allows us to study the contribution of each k_x, k_y GENE fluctuation to the synthetic signals. Since we are mainly interested in reproducing the relative amplitudes of the fluctuations we have chosen E_{p0} in the plane wave approximation Eq. (16) to obtain similar amplitudes to the Gaussian beam case.

As pointed out in subsection II A, the consequence of selecting the wave vector directions is also a reduction in the integration length. Under the assumption that the measured wave vector satisfies $\boldsymbol{k}_{\text{meas}} \parallel \boldsymbol{k}_0 \times \boldsymbol{B}$, each of the fluctuation components $\delta n_e(k_x, k_y, z(r_i, \ell))$ is a delta function, which is non-zero only at the point $\ell = \ell_\perp$ where that (k_x, k_y) component is perpendicular to the laser beam. If we set θ equal to the fast varying phase in Eq. (14), $\theta(k_x, k_y, r_i, \ell) = k_x x(r_i, \ell) + k_y y(r_i, \ell)$, we define $\ell_\perp$ such that

$$\frac{\partial \theta(k_x, k_y, r_i, \ell)}{\partial \ell}\bigg|_{\ell=\ell_\perp} =$$

$$k_x \frac{\partial x(r_i, \ell)}{\partial \ell}\bigg|_{\ell=\ell_\perp} + k_y \frac{\partial y(r_i, \ell)}{\partial \ell}\bigg|_{\ell=\ell_\perp}$$

$$= \left(k_x \nabla x(r_i, \ell) + k_y \nabla y(r_i, \ell)\right) \cdot \boldsymbol{e}_\ell\bigg|_{\ell=\ell_\perp}$$

$$= \boldsymbol{k}_\perp \cdot \boldsymbol{e}_\ell\bigg|_{\ell=\ell_\perp} = 0. \quad (19)$$

For purely radial modes with $k_y = 0$ this position is at the tangency point, $\ell_\perp = \ell_{\text{tangency}}$ as illustrated in Fig. 6. At a given point ℓ along the laser beam we therefore have contributions from all (k_x, k_y) modes that satisfy $k_x \nabla x(r, \ell) + k_y \nabla y(r, \ell) \parallel$
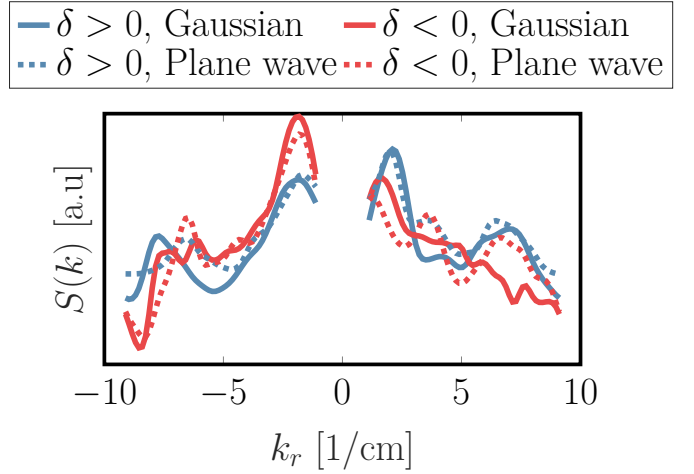

FIG. 12. Comparison of the wave-number spectrum when using either the proper approach with a Gaussian laser beam (solid lines) with the simplified approach of a plane wave (dashed lines). We show the comparison for both positive (blue) and negative (red) triangularities.

$\boldsymbol{k}_0 \times \boldsymbol{B}$. When the filter axis is along the radial direction at the tangency point, wave vectors that are mostly radial will contribute to the PCI signal, meaning that the contribution to the integral in Eq. (1) should mainly come from a small segment near the tangency point. In the next section we will ignore the assumption $\boldsymbol{k}_{\text{meas}} \parallel \boldsymbol{k}_0 \times \boldsymbol{B}$ and seek to rederive it directly, by estimating the "true" integration length we obtain and its relation to the dominant k_x, k_y components in the PCI signals.

IV. LOCALISATION OF THE SYNTHETIC SIGNALS

In this section we compute estimates of the "true" integration length and localisation. We compare our results with the theoretical expectation when the measured wave vector strictly satisfies $\boldsymbol{k}_{\text{meas}} \parallel \boldsymbol{k}_0 \times \boldsymbol{B}$, as was discussed in the previous Section II. First in subsection IV A we present the method we use for computing the localisation. Then in subsection IV B we illustrate the localisation for the positive and and negative triangularity discharges, presented in subsection III A.

A. Method for computing the localisation

When computing the localisation of the PCI signals we will rely on the simplified approach for computing the synthetic signals, described in subsection III B 2. This will allow us to study the localisation and the contribution of each individual GENE k_x and k_y fluctuation components and thus see the effect of the geometrical mode structure of the various contributions.

Localisation relies on the two criteria, $\boldsymbol{k}_{\text{meas}} \perp \boldsymbol{B}$ and

$\mathbf{k}_{\text{meas}} \perp \mathbf{k_0}$. The criterion $\mathbf{k}_{\text{meas}} \perp \mathbf{B}$ is already a built-in assumption in gyrokinetics and can be verified by noting that the variation along the parallel direction is much slower compared to the variation across a field line $\mathrm{dln}\,\delta n_e/\mathrm{d}z \ll \mathrm{dln}\,\delta n_e/\mathrm{d}x \sim \mathrm{dln}\,\delta n_e/\mathrm{d}y$. By representing the fluctuations in terms of their k_x and k_y wave numbers we therefore automatically consider fluctuations that satisfy $\mathbf{k}_{\text{meas}} = \mathbf{k}_{\perp,\mathbf{B}} \perp \mathbf{B}$. The wave vector perpendicular to the magnetic field, for every k_x and k_y, is given by

$$\boldsymbol{k}_{\perp,B}(\ell,r) = \nabla x(\ell,r)k_{x,\text{eff}}(\ell,r)$$
$$+ k_y C_y \left(q_0 \nabla \chi(\ell,r) - \nabla \phi(\ell,r) \right), \qquad (20)$$

where the effective radial wave number is $k_{x,\text{eff}}(\ell,r) = k_x + \chi(\ell)\hat{s}k_y$ and where the dependence on χ shows how the radial wave number increases as we move in the poloidal direction, due to the magnetic shear. This wave vector is a function of the coordinate along the beam due to the gradients, $\nabla x(\ell)$ and $\nabla y(\ell)$. Notice that $\boldsymbol{k}_{\perp,B}(\ell)$ is everywhere continuous while $\nabla y(\ell)$ has a jump once we cross the inner midplane. This is again a consequence of the parallel boundary conditions and the connection of the k_x modes, since the jumps in ∇y and k_x cancel.

The second property that the measured fluctuations have to satisfy is $\mathbf{k}_{\text{meas}} \perp \mathbf{k_0}$, and is a consequence of the line averaging. Away from $\ell = \ell_\perp$ a given k_x, k_y mode generates a large component along $\boldsymbol{k_0}$ and is therefore averaged over once we carry out the integration. This implies that the integral over the whole laser beam path L in Eq. 13 can be replaced by an integral over a shorter segment $\Delta L_{k_x,k_y}$ centred at $\ell = \ell_\perp$, provided that the rest term is small compared to the contribution around $\ell = \ell_\perp$. This property should be satisfied in a *statistical sense* such that the analysis of the PCI signals does not change when we integrate over the shorter segment. Since the analysis of the PCI signals is often performed by computing the Power-Spectral Density (PSD) we aim to find $\Delta L_{k_x,k_y}$ that preserves the PSD. We therefore compute the PSD of the cumulative integral around $\ell = \ell_\perp$ and sum over the frequency components to estimate the total power contribution from a given segment of length ΔL

$$S_{k_x,k_y}(r_i,\Delta L) = \left(\frac{\sqrt{\rho} c E_{p0}^2}{4\pi} r_e \lambda_0 M^2 \right)^2$$

$$\times \sum_f \left| \int_{\ell_\perp(k_x,k_y)-\Delta L/2}^{\ell_\perp(k_x,k_y)+\Delta L/2} \mathrm{d}\ell \hat{G} \mathscr{T}_{\text{av}} \delta n_{e_{k_x,k_y}}(z(r_i,\ell),f) \right|^2 \quad (21)$$

where

$$n_{e_{k_x,k_y}}(z(r_i,\ell),f) = \delta n_e(k_x,k_y,z(r_i,\ell),f)e^{ik_x x(r_i,\ell)+ik_y y(r_i,\ell)}$$

and where we have carried out a Fourier transform over the relevant frequencies f of the density fluctuations. In this case we consider f between 10 and 300 kHz which has been commonly used when analysing the PCI signals in this work.

If $\Delta L_{k_x,k_y}$ preserves the PSD it implies that for larger integration lengths, $\Delta L > \Delta L_{k_x,k_y}$, the value of $S_{k_x,k_y}(\Delta L)$ should

not change. We therefore define

$$\Delta L_{k_x,k_y} = \min(\Delta L):$$
$$\left| \frac{S_{k_x,k_y}(\Delta L_{k_x,ky})}{S_{k_x,k_y}(\Delta L)} - 1 \right|^2 \leq \varepsilon \,\, \forall \, \Delta L \geq \Delta L_{k_x,k_y}, \qquad (22)$$

where $\varepsilon = 0.1$, meaning that the reduced segment includes at least 90% of the total signal power. To illustrate this method we take as an example a purely radial $k_y = 0$ mode. A snapshot of the PCI signal from this component is shown in the top plot in Fig. 13, with and without applying a straight filter. The considered component is perpendicular to the PCI laser beam at the tangency point, $\ell_\perp \approx 0.3$ m. When evaluating Eq. (21) for this case we obtain the result in the bottom plot in Fig 13. The straight red thick lines in both plot shows the chosen integration length. It is clearly seen how the narrow straight filter suppresses the considered fluctuation component once its wave vector falls outside the filter, leading to a much more localised measurement. For a general PCI geometry we might
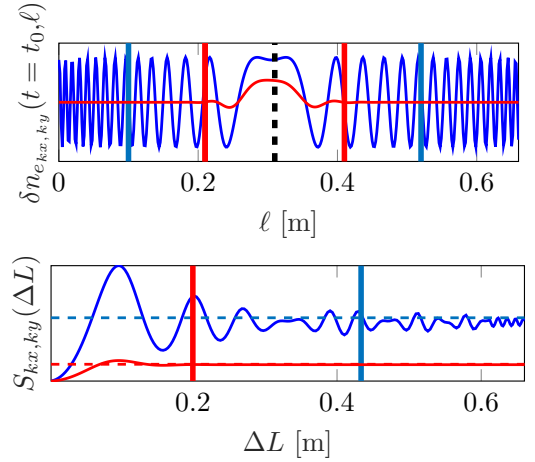

FIG. 13. On the top: Electron density fluctuation, along the central chord of the PCI beam ($r_i = r_0$) for a purely radial electron density fluctuation component $k_x \neq 0, k_y = 0$ without applying any filter (blue) and with a straight filter (red). The black dashed line indicates the $\ell_\perp$ point and the solid line for each component shows the calculated integration length. On the bottom: the result from Eq. (21) for both cases.

have multiple values of $\ell_\perp$ and therefore potentially multiple localised segments that should be taken into account when we carry out the integration. In this case we compute a value of $\Delta L_{k_x,k_y}$ separately for each segment by centering the integration interval in Eq. (21) around each $\ell_\perp$. In the next subsection IV B we will focus on the localisation of the PCI signals in TCV, where we only have a single segment. The case of multiple $\ell_\perp$ values will be discussed in detail later in Section V B where we will look at the PCI geometry proposed for JT-60SA.

We will carry out the analysis of the localisation for the central PCI ray only, with $r_i = r_0$, since other rays will lead to similar results. In the following it is assumed that all quan-

tities are evaluated at $r_i = r_0$ and we henceforth omit writing this variable to simplify the notation.

There are three different features of the density fluctuation in Eq. (14) that can have an effect on the localisation. The most important is localisation due to the geometrical structure of a k_x and k_y mode. To study this we assume that the electron density fluctuation takes the form

$$\delta n_e(\ell)_{k_x,k_y} = e^{i\left(k_x x(\ell)+k_y y(\ell)\right)} = e^{i\theta(k_x,k_y,\ell)} \quad (23)$$

with constant fluctuation amplitude along the laser beam. The subscript indicates that we now consider just one k_x, k_y fluctuating component. Fluctuations of the form described by Eq. (23) have been the basic assumption in the past when making estimates of the PCI localisation[25–27]. The result in this case can be compared with an estimate of the integration length which is derived by performing a second order Taylor expansion of the fast-varying phase θ around the tangency point $\ell_\perp$

$$\theta(k_x,k_y,\ell) \sim \theta(k_x,k_y,\ell_\perp)$$
$$+\frac{1}{2}\frac{\partial^2\theta(k_x,k_y,\ell)}{\partial\ell^2}\bigg|_{\ell=\ell_\perp}(l_\perp-l)^2,$$

where we used Eq. (19) to remove the first order derivative. For some constant C we thus find

$$\Delta L_{k_x,k_y} \sim \sqrt{2C\left/\left|\partial^2\theta(k_x,k_y,\ell)\left/\partial\ell^2\right|_{\ell=\ell_\perp}\right|\right.}. \quad (24)$$

The value of C is chosen such that $\Delta L_{k_x,k_y}$ calculated through Eq. (24) matches Eq. (22) at low $k_\perp \sim 1$ cm^{-1}.

In addition to the geometrical structure described by the fast varying phase in Eq. (23) there are two more features of the fluctuations that have to be taken into account for a proper estimate of the localisation. The first is the effect of the phase of the complex Fourier amplitudes, $\hat{\theta}(k_x,k_y,\ell,t)$, which can be defined from the relation

$$e^{i\hat{\theta}(k_x,k_y,\ell,t)} = \delta n_e(\ell,t)_{k_x,k_y}\left/\left(\left|\delta n_e(\ell,t)_{k_x,k_y}\right|e^{i\theta(k_x,k_y,\ell)}\right)\right. (25)$$

This phase is in general dependent both on time and position along the beam, and reflects the field aligned nature of the fluctuations. The more realistic signal thus becomes

$$\delta n_e(\ell,t)_{k_x,k_y} = e^{i\hat{\theta}(k_x,k_y,\ell,t)}e^{i\theta(k_x,k_y,\ell)}. \quad (26)$$

Finally, we can also have a time and spatial variation of the Fourier amplitude $\left|n_e(\ell,t)_{k_x,k_y}\right|$, which in a local simulation mainly reflects the ballooning structure of the fluctuations. The actual simulated fluctuations thus take the form

$$\delta n_e(\ell,t)_{k_x,k_y} =$$
$$\left|\delta n_e(k_x,k_y,z,t)\right|e^{i\hat{\theta}(k_x,k_y,\ell,t)}e^{i\theta(k_x,k_y,\ell)}, \quad (27)$$

which is equal to Eq. (14) when only considering a single k_x, k_y mode. The effect of both the phase ϕ and the spatial variation of the Fourier amplitudes can only be addressed in part in a local simulation. In reality, both amplitude and phase will

vary along the laser beam due to variation in the background profiles and their gradients, as well as change in the magnetic geometry. These effects could properly be addressed with a global simulation, but in this work we limit the analysis to the local case, while a comparison with a global simulation is left for future work.

B. Localisation for positive and negative triangularity TCV plasmas

We focus the analysis of the localisation properties for TCV on the positive triangularity case, and in the end we make a comparison with results for the negative triangularity case. We carry out the exercise of calculating $\Delta L_{k_x,k_y}$ for all three forms of the density fluctuations, and with and without applying the filter in Eq. (21). We illustrate the localisation properties for two different filter angles: 160 degrees and 100 degrees (the angle is calculated relative to the outer plasma midplane). For the positive triangularity discharge, #49052, a 160 degree filter angle corresponds to the radial direction at the tangency point. A straight filter with a width equal to the Gaussian width of the focal spot will be compared with the wedge filter. The wedge half angle is $\theta_W = 30$ degrees, which has been commonly used in the experiments. We will consider only the main fluctuating components falling inside the filter, whose power is larger than 1% of the RMS value when averaging over all k_x, k_y contributions.

For the positive triangularity case and a 160 degree filter angle we obtain the power levels as shown in the two first columns in Fig. 14. The top row (a) includes only geometrical effects (i.e a density fluctuation given by Eq. (23)) while the middle row (b) also includes the effect of the phase, Eq. (26). In the third row (c) we show the result obtained when considering the true form of the simulated density fluctuation, Eq. (27), but normalised by its RMS value. Finally, the actual simulated, unnormalised, fluctuations have been used to obtain the result in the bottom row (d). For a 160 degree filter angle the filters clearly preferably select components with low k_y. In the case of Eq. (23) the $k_y = 0$ component is perfectly symmetrical, while there is a very slight asymmetry appearing for larger k_y. Adding the effect of the phase $\hat{\theta}$, Eq. (26), leads to a slight asymmetry in the $k_y = 0$ components that have now a dominant contribution that is propagating radially outward, $k_x > 0$. When using Eq. (27), the $k_y = 0$ component stands out even more and finally, when including the actual amplitude it clearly becomes the dominant feature in the PCI signal. As will be shown in the next section, V A, this component in fact corresponds to a radially outward propagating GAM and is dominating the synthetic PCI signals for the considered positive triangularity TCV scenario.

Next, in Fig. 15, we show the corresponding localisation along the laser beam, after applying Eq. (21) and using the criterion in Eq. (22), for each type of density fluctuation. Instead of ΔL we show the equivalent segment length in $\Delta\rho_{k_x,k_y}$, i.e the corresponding extent of the segments across the flux surfaces. The case without any filter (red circles) tests the property, $k_{meas} \perp k_0$ which we can see is poorly satisfied.

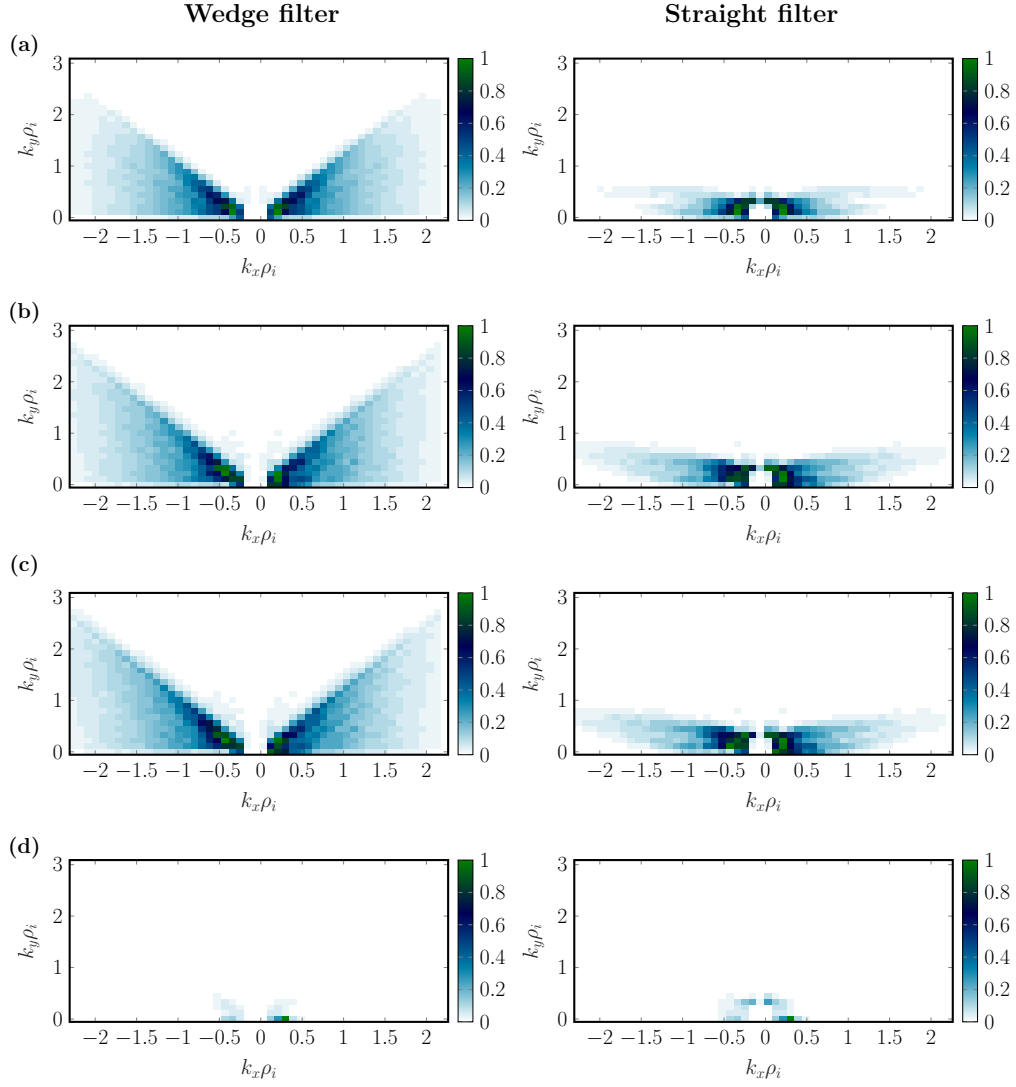**Wedge filter**   **Straight filter**

FIG. 14. Total power of each GENE k_x, k_y component when integrated over the whole laser beam propagation length in the case of a wedge filter (first column) and a straight filter (second column). The fluctuating data used to generate these plots comes from the positive triangularity case, discharge #49052. Both filters have a filter angle equal to 160 degrees, which corresponds to the radial direction at the tangency point. The power levels are shown of a density fluctuation of the form given in Eq. (23), (a), when including the effect of the phase $\hat{\theta}(k_x, k_y, \ell, t)$, Eq. (26) (b) when considering the actual simulated density fluctuation but normalised with its RMS value, Eq. (27) (c), and finally when including the actual amplitude of the simulated density fluctuations (d). The color scale is such that darker green colors indicate large amplitudes.

For $k_\perp(\ell_\perp) < 7$ cm^{-1} essentially the whole laser beam path length, $\Delta\rho_{k_x,k_y} \sim 0.4$, is required to be able to reproduce a power level above 90% of the actual value. For increasing $k_\perp(\ell_\perp)$ however we start to see a reduction in the integration length. This indicates that the spatial variation of the fluctuation is fast enough and the contribution to the PSD away from $\ell = \ell_\perp(k_x, k_y)$ is being averaged out. Applying a wedge filter (blue squares) leads to only slightly better localisation at low $k_\perp$. We conclude that while the wedge filter does have the effect of restricting the wave-vector directions, it has nonetheless little effect on the localisation. Very good localisation is however seen when we consider the optimal case, i.e apply a straight filter (green asterisks). Most components in this case have $\Delta\rho_{k_x,k_y} \sim 0.1$. In the straight filter case, lighter shades

of green indicates an increase in the k_y wave number which seems to lead to worse localisation. The reason is that the $\ell_\perp$ locations of $k_y \neq 0$ components are away from the tangency point, where ρ and the angle between the fluctuation wave vector and laser beam is varying the most. For $k_y \neq 0$ the same integration length along the laser beam path thus translates to a larger $\Delta\rho_{k_x,k_y}$. The different values of k_y are also responsible for the large spread seen in the unfiltered case. Finally, with black crosses we compare our calculated localisation with the simple estimate given by Eq. (24). We see that it agrees well with the trend of the unfiltered case, and even with the case of a wedge filter.

The localisation is similar for all three forms of the density fluctuation, Eq (23), Eq (26) and Eq (27), with the main dif-
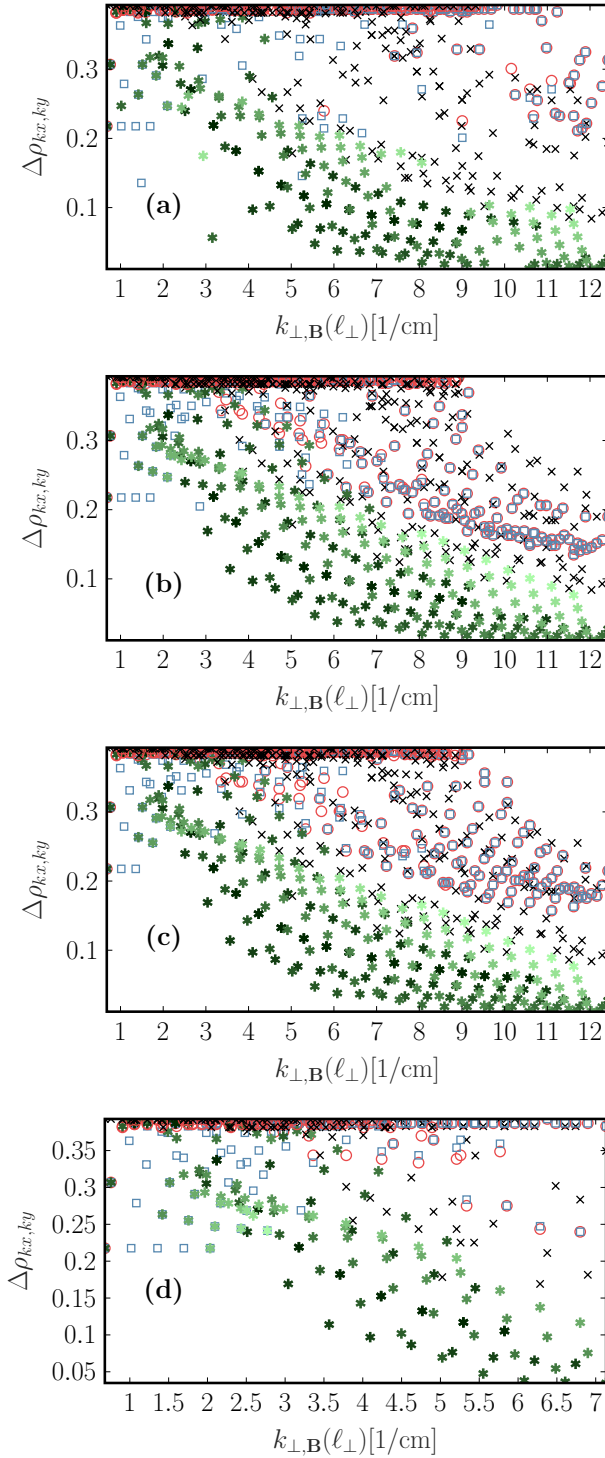
FIG. 15. The localisation in terms of the radial coordinate $\Delta\rho_{k_x,k_y}$ after applying Eq. (21) and using the criterion in Eq. (22) for the components. The four boxes correspond to the four rows in Fig. 14. We show the unfiltered (red circles), the wedge filter (blue squares) and the straight filter (green stars) case. A comparison is done with the estimated integration length calculated from Eq. (24) (black crosses). For the straight filter case, the color gradient indicates different values of k_y; dark colors corresponds to low values of k_y while lighter colors show an increase in k_y.

ference coming from the fact that in the latter two fewer components are considered in the calculation of the localisation, because of their very low amplitudes. In the actual synthetic signal, as shown in subfigure (d), most components have a relatively low value of $k_{\perp,B}(\ell) < 8 \text{ cm}^{-1}$.

If we rotate the filter by 60 degrees, to a 100 degrees angle, we obtain the power levels shown in Fig. 16 and the corresponding localisation as shown in Fig. 17. The $k_y = 0$ components are not at all included now and the form of the PCI signals is essentially dictated by the poloidal $k_y \neq 0$ fluctuating components. The lighter green colors for the straight filter case now indicate an increase in $k_{\perp,B}(\ell_\perp)$. Thus, unlike Fig. 15, increasing $k_{\perp,B}(\ell_\perp)$ corresponds now to an increase in k_y rather than an increase in k_x as was previously the case. The localisation for this filter configuration is considerably worse, than in the case of the other filter configurations, which included a large fraction of k_x values. The absence of any markers in the case of the filter for $k_{\perp,B}(\ell_\perp) > 8 \text{ cm}^{-1}$ shows how restrictive this filter configuration is. When including the effect of phase and amplitudes, a radially outward component with $k_y\rho_i \sim 1$ becomes dominant. Although we get worse localisation, in this configuration TPCI can be used to study ITG and TEM turbulence. The configuration used in Fig. 15 is instead more appropriate for studying purely radially propagating modes with $k_y = 0$, such as the GAM.

All of these results have to this point been computed for the positive triangularity case only. We illustrate also the corresponding results for the $\delta < 0$ case, using a 160 degree filter angle. Due to the change in the magnetic geometry, this filter angle no longer corresponds to the radial direction at the tangency point. Consequently, as shown in Fig. 18, the localisation is worse than for the corresponding positive triangularity case, Fig. 15. The power levels in Fig. 19 show that the filters still include $k_y = 0$ components, but poloidal components with $k_y \neq 0$, propagating radially inward, are favoured in the measurement. Because of these k_y components, the signals in the negative triangularity case have lesser localisation. Notice that larger k_x values in the case of a straight filter (seen by following the green markers with a constant color) lead to slightly worse localisation. This is because in this particular case the larger k_x components stay within the filter for a slightly longer length along the laser beam. This effect is most visible for the larger k_y values (lighter green colors). From the plots of the PSD levels, it is clear that, unless the raw fluctuation data contains a strong purely radial component, the measurement will be dominated by $k_y > 0$ components, propagating radially inward.

To conclude, in contrast to past predictions of the PCI localisation[26,28,29] we find that the property $\boldsymbol{k}_{\text{meas}} \perp \boldsymbol{k}_0$ is not perfectly satisfied and consequently the localisation is not as good as previously believed when no spatial filter is used. Also, while in the case of a narrow straight filter the localisation is indeed very good, especially in the radial coordinate, the wedge filter, which has also been commonly used in the experiments, provides relatively poor localisation. For this case, stating that the signal only comes from the tangency point is therefore inaccurate. It is interesting to note that the increasing complexity in the description of the density fluctuations

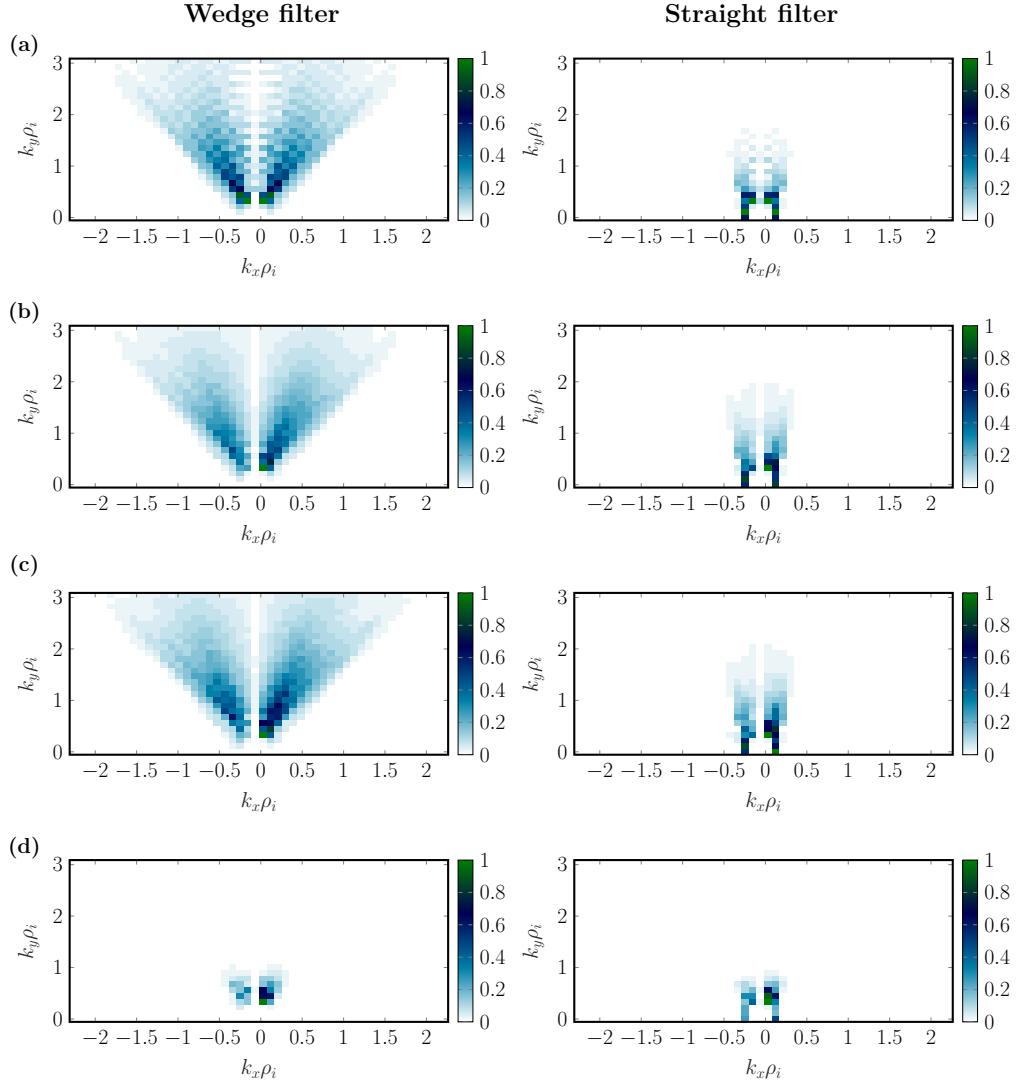**Wedge filter**   **Straight filter**

FIG. 16. Same as Fig. 14 but for the case of a 100 degree filter angle.

(including phase and amplitudes) has little effect on the localisation. This could mean that global effects also will play little role on the localisation. However, this does not mean that global effects can be neglected. For example, the contribution to the PCI signals could be localised to a portion of the plasma where fluctuation levels are small (such as close to the core) which can only properly be accounted for by making a global simulation.

V. A FIRST INTERPRETATION AND PREDICTION OF EXPERIMENTAL PCI MEASUREMENTS WITH THE SYNTHETIC DIAGNOSTIC

In this section we use the tools presented in the past sections to interpret and predict actual PCI measurements. First in subsection V A we use the synthetic diagnostic to interpret past PCI measurements of two discharges at TCV, carried out to study the effect of plasma shaping on turbulence. Then in

subsection V B we study the characteristics of the different PCI set-up that is envisioned for JT-60SA. We will discuss the localisation properties for this case and make first predictions of the expected PCI signals.

A. Interpretation of PCI measurements at TCV

We will begin by presenting the results with the synthetic diagnostic. Then we will show the corresponding experimental results and make a comparison between the two.

We consider the two discharges #49052 and #49051, with positive and negative triangularity respectively and equal ECH power, that were carried out in the past to study the effect of triangularity in TCV[30]. These discharges were already introduced in Section III A. For modelling the TPCI signal we take the electron density fluctuations obtained from the GENE simulations when using the parameters in Table I, and post-process them with the synthetic diagnostic, using the method

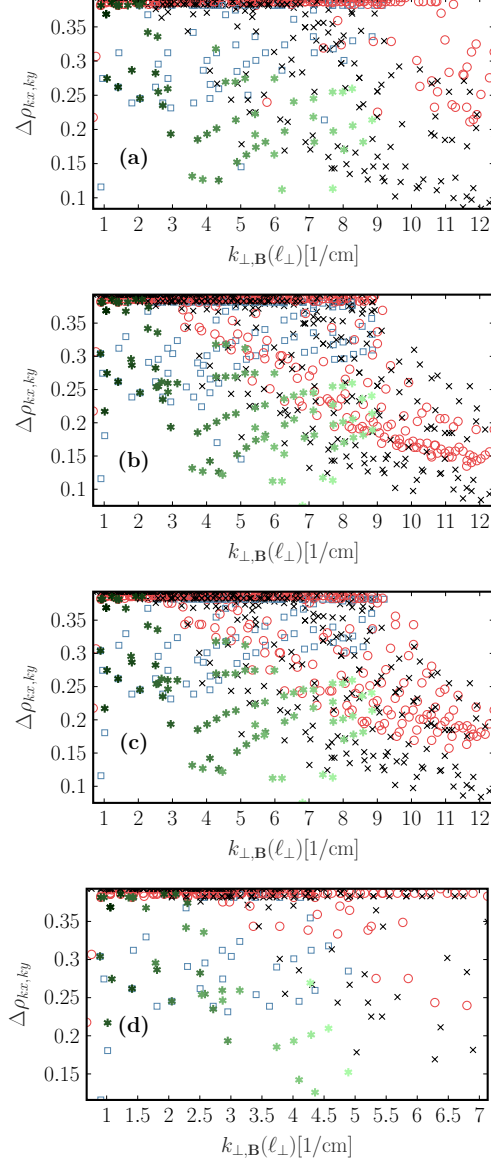FIG. 17. Same as Fig. 15 but for the case of a 100 degree filter angle.

FIG. 18. Same as Fig. 15 but for the negative triangularity case.

described in Section III B. The set-up of the diagnostic is the same as used in the corresponding experiments: nine unevenly spaced detector elements (and therefore nine values of $r = r_1, r_2 \dots r_9$), with a 5 cm diameter beam. The lower wavenumber cut-off is at $k_c = 1.01$ cm^{-1} and the maximum measurable wave number is at $\max(k_r) \sim 9$ cm^{-1}. The spatial filter is a wedge with half angle $\theta_W = 30$ degrees and oriented along the radial direction at the tangency point (160 degree filter angle).

First, directly from the analysis carried out in subsection IV we can conclude that the integration length for this case will be similar to the unfiltered case, shown in blue in Fig. 15, with $\Delta \rho_{k_x, k_y} \approx 0.3$ which essentially corresponds to the whole laser beam propagation length ≈ 50 cm, at the maximum (Nyquist)

wave number frequency $|\boldsymbol{k}_{\perp, B}|$. As already mentioned in the previous section, the consequence of this is that the contribution to the PCI signal is coming from the whole laser beam path and not only the tangency point. This both complicates the interpretation of the TPCI results and makes the flux tube approximation less appropriate for modelling the PCI signals. Since a global simulation that would generate sufficient time statistics is still outside the scope of this paper, we continue with the flux tube approximation. As we will see, even in this case the synthetic diagnostic is able to reproduce the main features seen in the corresponding experimental signals.

The wave-number spectrum and frequency spectrum of the synthetic data are shown in Fig. 20 for both the positive and

Wedge filter   **Straight filter**
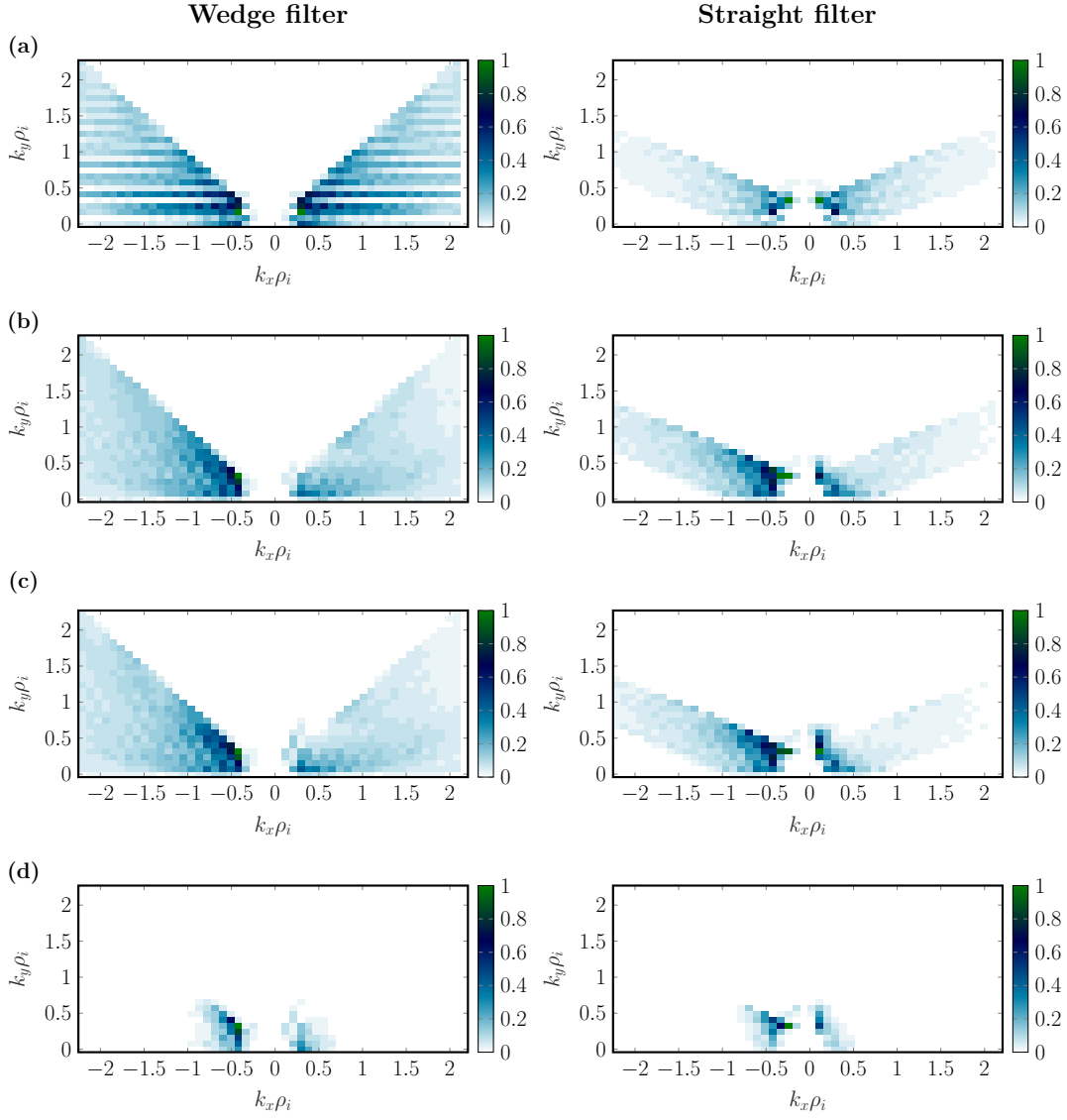
(a)

(b)

(c)

(d)

FIG. 19. Same as Fig. 14 but for the negative triangularity case.

negative triangularity cases. We use the plane wave approximation and compare between different contributions to the PCI signals. We either include all k_x and k_y components in the sum in Eq (16), only purely radial components with $k_y = 0$ or finally only components with a non-zero binormal wave number, $k_y \neq 0$. This is a convenient way to split the contributions since $k_y = 0$ corresponds to purely zonal type modes, while $k_y \neq 0$ includes contributions from non-zonal modes only, such as ITG modes and TEM.

The wave-number spectrum in Fig. 20 $S(k_r)$ for $\delta > 0$ (a) suggest that the density fluctuations propagate mostly outward, $k_r > 0$, with most of the contribution coming from $k_r \sim 2$ cm^{-1}. We can see that this corresponds to the purely radial $k_y = 0$ fluctuation contributions. Notice that the dominance of this component in the synthetic result was already predicted from the plots of the PSD in Fig. 15. The $k_y = 0$ components also lead to a peak in frequency at $F \sim 40$ kHz,

which is typical for a Geodesic Acoustic Mode (GAM) in TCV[31]. An analysis of the raw GENE output has revealed that the $k_y = 0$ density fluctuation component has indeed the poloidal $m = 1$ structure of a GAM. Although $k_y = 0$ provides the dominant contribution in the $\delta > 0$ case, modes with $k_y \neq 0$ are instead responsible for a power cascade in frequency as shown in the frequency spectrum $S(f)$ in Fig. 20.

The asymmetry of the $k_y = 0$ component is due to the structure of the complex Fourier amplitudes of the raw density fluctuations generated by GENE, combined to the effect of the measurement geometry. This was already suggested by the rows (b,c) in Fig. 15. If we look at the frequency and k_x spectra of the $k_y = 0$ components coming from the raw GENE density fluctuations we notice that the $k_x > 0$ components are dominant in the upper midplane, $z > 0$, as shown in Fig. 21. In a flux tube the $k_y = 0$ component has to satisfy the symmetry[32] $\Phi(k_x, z) = \Phi(-k_x, -z)$. Therefore if averaging over the whole
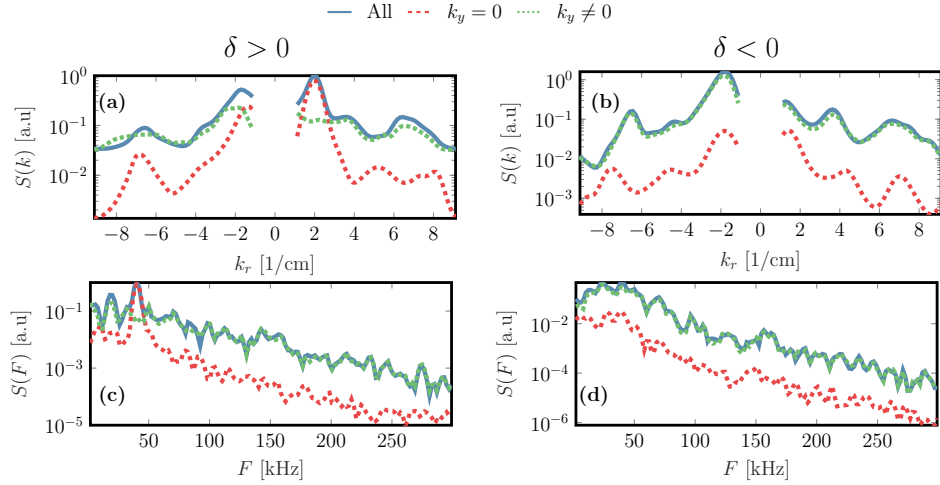
FIG. 20. Synthetic wave-number spectrum (top), frequency spectrum (bottom) for $\delta > 0$ (left) and $\delta < 0$ (right) cases. The result is shown when including all k_y contributions in Eq. (16) (solid blue), only $k_y = 0$ (dashed red) and only $k_y \neq 0$ (dotted green).

flux surface the GAM will not have any preferential propagation direction. However, in our case the TPCI laser beam only passes through the upper midplane of the plasma, as was shown in Fig. 4. This means that the PCI beam picks up only the dominant $k_x > 0$ component of the $k_y = 0$ fluctuations, explaining the asymmetry seen in Fig. 15 and Fig. 20. Instead, if the TPCI beam passed through the lower midplane, it would pick up the dominant $k_x < 0$ component and the wave-number spectrum $S(k)$ in Fig. 20 (a) would show the opposite propagation direction for the dominant $k_y = 0$ component.

Contrary to $\delta > 0$, fluctuations seem to propagate radially inward for the negative triangularity $\delta < 0$ case. This is suggested by the wave-number spectrum $S(k_r)$ shown in the bottom row in Fig. 20 that has a dominant component now at $k_r \approx -2$ cm^{-1}. It is also clear that the zonal $k_y = 0$ component makes a very modest contribution and the signal is almost entirely dominated by fluctuations with $k_y \neq 0$. Based on the results in Fig. 18 we can directly conclude that the low contribution of $k_y = 0$ components is both due to the different plasma geometry and different characteristics of the fluctuations. Indeed it is clearly seen in Fig. 22 that the amplitudes of the $k_y = 0$ component in the upper midplane are significantly smaller than in the $\delta > 0$ case. There is also no clear GAM structure, which was the reason for the positive k_x asymmetry seen for the $\delta > 0$ case. Indeed this explain the synthetic results, but we stress that we do not yet have an understanding of what makes the GAM contribution disappear in the $\delta < 0$ case.

More details on the fluctuations in the PCI signals are given by the conditional wave-number and frequency spectrum $S(k_r|f)$ which is shown in Fig. 23, and is defined as the spatial Fourier transform of the complex coherence function $C(\Delta r, f)$. In addition to the plane wave approximation we also show the synthetic result when using the true, gaussian beam approach. Apart from a very slight difference in some frequency and wave-number components we see that the two approaches give very similar results. There is a slightly larger

frequency spread in the Gaussian beam case, and the left leg with $k_r < 0$ is also more prominent.

We now show the results from the corresponding actual TPCI measurement. The conditional wave-number and frequency spectra for the $\delta > 0$ case and for $\delta < 0$ are shown in Fig. 24. In the $\delta > 0$ case the measurement is clearly dominated by fluctuating components with $k_r > 0$, with the largest component having $k_r \sim 2$ cm^{-1} and $F \sim 40$ kHz. The negative triangularity case on the other hand is dominated by components with $k_r < 0$. All these observations are in good agreement with the results we saw from the modelling with the synthetic diagnostic in Fig. 23. Our interpretation of the difference between measurements in $\delta > 0$ and $\delta < 0$ is therefore a change in the contribution from the GAM mode. While the wave number of the dominant contribution is in good agreement with experiments, more analysis is required to understand the larger frequency spread seen in the experimental case. A potential explanation could be a variation of the GAM frequency due to global effects, which could not be captured by the local analysis performed here.

In conclusion we have seen that the synthetic diagnostic appears to be able to reproduce the main signatures of the PCI signals, in particular the change in the TPCI $S(k_r)$ spectra when we transition from $\delta > 0$ to $\delta < 0$. More detailed gyrokinetic simulations, varying input parameters and radial positions, are required to better understand the difference between synthetic and experimental results.

B. First prediction of TPCI measurements for JT-60SA

In a recent publication[27] a design for a PCI system for the JT-60SA tokamak was proposed. The proposed PCI design features a tangentially viewing geometry, similar to TCV, but with a laser beam that passes deeper into the plasma cross-section, as is depicted in Fig. 25. The corresponding radial coordinate ρ along the laser beam is shown in Fig. 26 (a).

$\delta > 0$

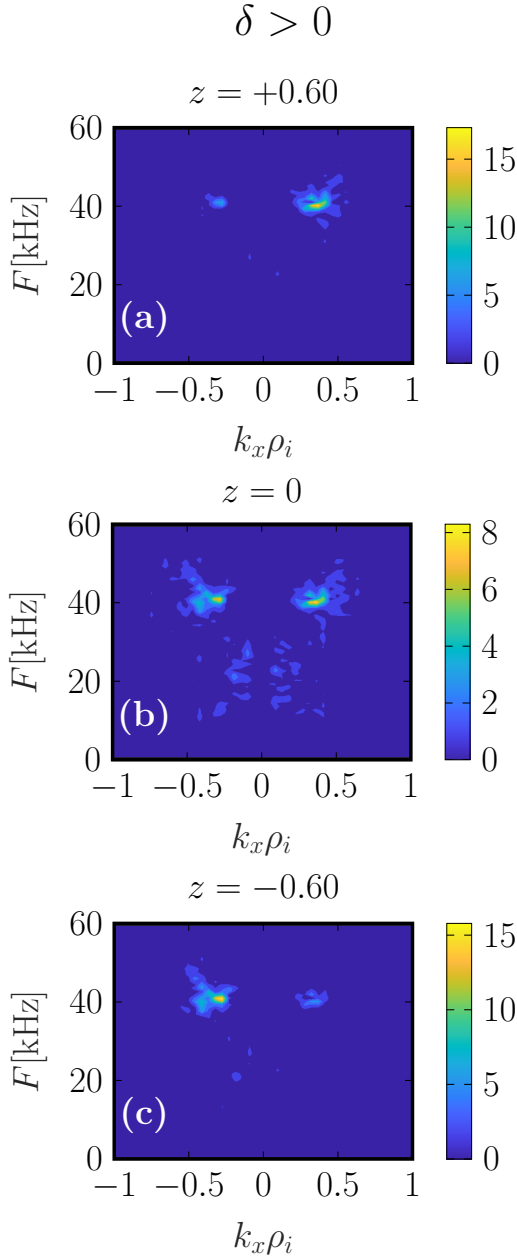$z = +0.60$

(a)

$z = 0$

(b)

$z = -0.60$

(c)

FIG. 21. The k_x and frequency spectra of the raw GENE $k_y = 0$ density fluctuation component, for $\delta > 0$. The spectrum is shown on the upper midplane (a), at the midplane (b) and on the lower midplane (c).

$\delta < 0$

$z = +0.60$

FIG. 22. The k_x and frequency spectra of the raw GENE $k_y = 0$ density fluctuation component, for $\delta < 0$, on the upper midplane.

we show the angle between the filter axis and the wave vector of the fluctuations $\boldsymbol{k}_{\perp,B}$, $\theta_{\boldsymbol{k}_{\perp,B},\boldsymbol{f}}$. In the optimal case of a narrow straight filter a fluctuating k_x, k_y component requires $\theta_{\boldsymbol{k}_{\perp,B},\boldsymbol{f}} \sim 0$ to scatter the laser light into the filter. In theory, to contribute to the PCI measurement we need simultaneously to satisfy $\theta_{\boldsymbol{k}_{\perp,B},\boldsymbol{f}} \sim 0$ and $\theta_{\boldsymbol{k}_{\perp,B},k_0} \sim 90$ degrees. By changing the filter orientation this means that we can either include the two regions near $\rho \sim 0.1$ (see blue line) or the single region near the plasma edge (see green line). In reality, as we will see in the following, for a given filter configuration there can still be a non-negligible contribution simultaneously from all three segments. However, the dominant contribution is still coming from either the two double segments or the single segmented region.

Notice the very sharp variation of both angles in Fig. 26 (b) and (c) in the double segmented regions. A very sharp variation in $\theta_{\boldsymbol{k}_{\perp,B},\boldsymbol{f}}$ means that the fluctuating component quickly falls outside the filter and the localisation is therefore very good. However, a very sharp variation in $\theta_{\boldsymbol{k}_{\perp,B},k_0}$ means, in principle, that unless $k_{\perp,B}$ is sufficiently large, the contribution from that location (either of the double segmented regions) will average out. In contrast, there is a much slower variation in both angles for the single segmented region near the HFS edge. This segment is thus better defined both in terms of the localisation length and in terms of the directions of $k_\perp$ that contribute to the measurement. As we will see in the following, for this case, we select mainly purely radial fluctuating components

To study the localisation properties and make first predictions of PCI measurements in JT-60SA we focus on a high-performance discharge, the so-called scenario 1, featuring a double-null separatrix, 41 MW neutral beam injection (NBI) and ECH, plasma current 2.3 MA, toroidal field on axis 1.7 T, safety factor at 95% of the minor radius $q_{95} = 5.6$, and normalised ratio of the plasma kinetic to magnetic pressure $\beta_N = 3.43$. The chosen radial location of the simulation was the result of a compromise: the regions of optimal TPCI localisation are the pedestal and the magnetic axis, the for-

In contrast to TCV, the beam in JT-60SA passes entirely, and multiple times, across the entire cross-section, leading to multiple locations $\ell_\perp$ where the considered k_x and k_y fluctuation component is perpendicular to the laser beam. These locations are illustrated in Fig. 26 (b) for $k_y = 0$ modes and correspond to when the angle between the laser beam and the wave vector of the fluctuations is $\theta_{\boldsymbol{k}_{\perp,B},k_0} \sim 90$ degrees. Two of these locations are near the core, $\rho \sim 0.1$, positioned on the LFS and HFS respectively, and a third is at $\rho \sim 0.8$ on the HFS. These different regions are also illustrated in Fig. 25. In Fig. 26 (c)
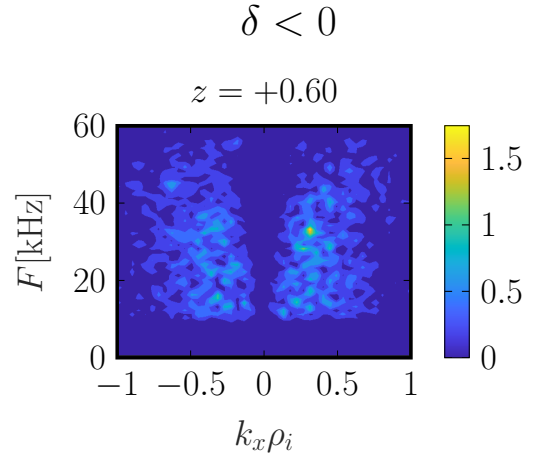
$\delta > 0$ $\delta < 0$

Synt., Plane wave   **Synt., Plane wave**

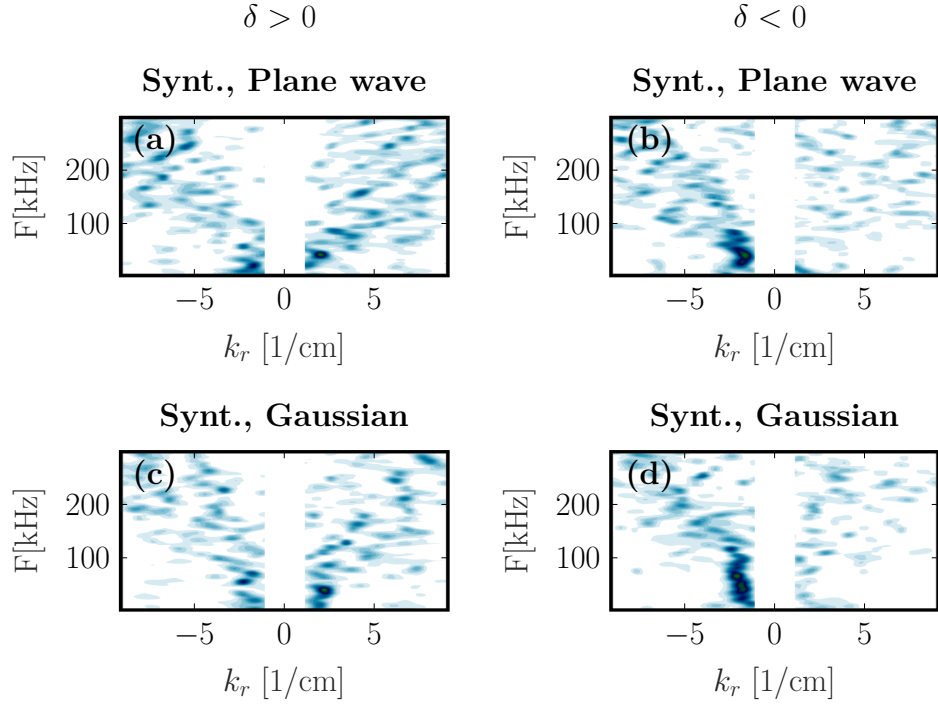**Synt., Gaussian**   **Synt., Gaussian**

FIG. 23. The conditional spectrum for $\delta > 0$ (left column) and $\delta < 0$ (right column). The top row (a,b) shows the synthetic results when using the plane wave approximation and the bottom row (c,d), shows the synthetic results when using the approach of a Gaussian laser beam.
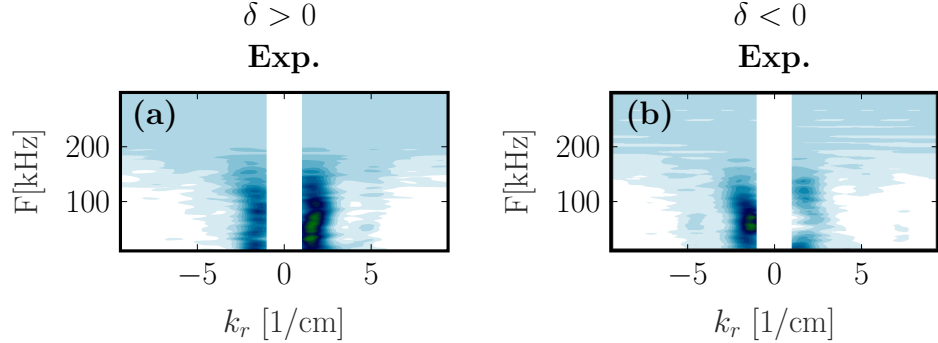
$\delta > 0$ $\delta < 0$

Exp.   **Exp.**

FIG. 24. Same as Fig 23 but calculated from the actual TPCI measurement in the $\delta > 0$ #49052 discharge (a) and $\delta < 0$ #49051 discharge (b).

mer typically requiring prohibitively large computational resources, and the latter featuring small pressure gradients and broadly stable conditions; we thus chose the innermost region with sufficient turbulence levels, roughly corresponding to mid-radius $\rho_t = 0.6$. The simulations for this scenario are part of a dedicated project with the objective of accurately modeling the turbulence in JT-60SA. The simulation includes collisions, Carbon impurities and fast ions modelled with an equivalent Maxwellian, as well as electromagnetic effects including compressional magnetic field fluctuations. The input parameters to the GENE simulations are summarized in Table II. The reference electron density at $\rho_t = 0.6$ is $n_e = 5.87 \times 10^{19}$ m^{-3}, the electron temperature is $T = 6.27$ keV and the minor radius is $r_a = 1.58$ m. We considered the resolution $N_x \times N_y \times N_z \times N_{v_{\parallel}} \times N_\mu \times N_s = 192 \times 32 \times 48 \times 32 \times 10 \times 4$.

The flux tube has a radial length $L_x = 127\rho_i$ and the binormal length $L_y = 62\rho_i$. A detailed presentation of the gyrokinetic results for this scenario is planned for a future publication. In the present analysis we will just use these gyrokinetic results in the synthetic diagnostic to make a first prediction for PCI measurements in JT-60SA.

First, we estimate the localisation and compute the contribution from the different k_x and k_y fluctuating components to the PSD of the PCI signals. We apply the same method as in Section IV for a given k_x and k_y component and consider the central ray only, $r = r_0$. We consider the two filter orientations already presented in Fig. 26 to show the results obtained when the contribution to the PCI signals is coming mostly from the single segmented region ($\theta_f = 0$) or from the two double segmented regions ($\theta_f = 90$ degrees). To simplify, we will only
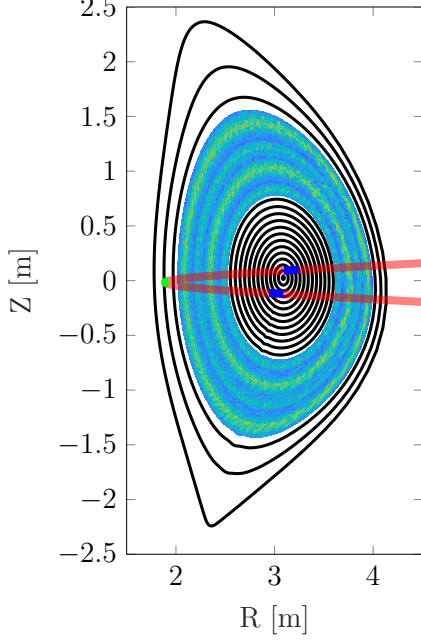
FIG. 25. The double-null geometry of the considered JT-60SA scenario together with the central ray of the PCI laser beam path shown in red. The blue segments illustrate the location of the double segmented regions while the green segment shows the single segmented region.

TABLE II. Parameters of the considered JT60SA scenario at $\rho_t = 0.6$ used as input to the GENE simulations, obtained from the MHD equilibrium code CHEASE[22] and species profiles. The parameter r_a is the local minor radius and R is the major radius.

T_D/T_e	1.0	$r_a/L_{n,C}$	0.7224	q_0	1.1571
$r_a/L_{T,e}$	2.512	$r_a/L_{n,FD}$	1.7231	$\hat{s}$	1.5528
n_D/n_e	0.7671	$r_a/L_{T,D}$	2.931	T_{FD}/T_e	8
$\varepsilon = r/R$	0.51	n_C/n_e	0.033	$r_a/L_{n,e}$	0.867
$Z_{\rm eff}$	2.0	n_{FD}/n_e	0.033	$a/L_{n,i}$	0.86782
β_e	2.4 %	$r_a/L_{T,FD}$	4.25	$v_c[10^{-3}]$	0.91

study the effect of geometry, thus using density fluctuations of the form (23), and compare it to the case when using the actual simulated density fluctuations of the form of Eq. (27).

Note that the passage of the PCI laser beam through the inner midplane leads to a jump in the χ and y coordinates. However both $k_{\perp,B}$, given by Eq. (20) and the synthetic signal in Eq. (16) are in fact continuous as a result of the parallel boundary condition and the correction connection of the k_x modes. Typically, in a non-linear simulation N_{k_x} is large enough that
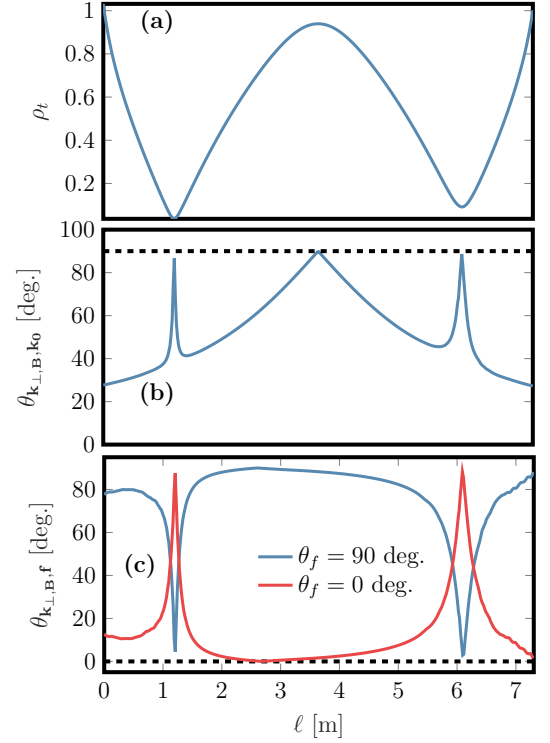

FIG. 26. The radial flux coordinate ρ_t as a function of the linear coordinate ℓ along the proposed JT-60SA PCI laser beam (a). In (b) we show the angle $\theta_{k_{\perp,B},k_0}$ between the wave vector of the fluctuations $k_{\perp,B}$ and the laser beam direction k_0, when considering a purely radial fluctuating component with $k_y = 0$. The black dashed line indicates a 90 degree angle. Finally (c) shows the angle $\theta_{k_{\perp,B},f}$ between the filter axis and the wave vector of the fluctuations, again just for the $k_y = 0$ component. Here the dashed black lines indicates a 0 degree angle. The latter is shown for two filter orientations, $\theta_f = 0$ (red) and $\theta_f = 90$ degrees (blue).

k_y modes with large amplitude have at least one connection between different k_x modes. The larger k_y modes with smaller amplitude instead have no connection. For a meaningful estimate of the localisation we need a continuous signal when we cross the midplane, and thus we only consider the k_x and k_y components for which there exists a k_x connection. In the considered GENE simulation the maximum binormal wave number that still has a connection between different k_x values is $k_y\rho_i = 0.91$. Fluctuating components with large k_x and k_y have very low fluctuating amplitudes and thus make a negligible contribution to the PCI signals and can safely be ignored when analysing the localisation properties of TPCI.

The PSD levels without applying any filter are shown in Fig. 27. The result is only shown for the k_x, k_y modes with an existing connection, whereas the other components are set to zero. As just mentioned, in any case these components only make a small contribution to the synthetic PCI signals due to their low fluctuation amplitudes. The remaining components have a dominant contribution around $k_y \sim 0.4$. From the actual case, Fig. 27 (b) we see that the simulation is dominated by modes at $k_y \sim 0.3$.
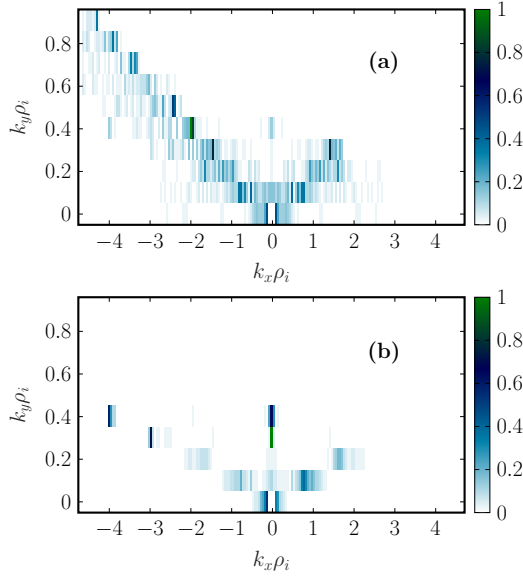
FIG. 27. PSD of each k_x, k_y component when integrating over the full JT-60SA laser beam path in the unfiltered case. Subfigure (a) shows the effect of the phase θ only, thus a density fluctuation of the form of Eq. (23) while (b) shows the actual simulated case, using Eq. (27). Only k_x, k_y modes with a connection are shown whereas the other components are set to zero.

We apply then a wedge filter, with a 30 degree half angle (thus the same as has been generally used in TCV thus far), as well as the straight filter with a width equal to the width of the focal spot, thus yielding the optimal localisation as in the case of TCV in Section IV. First, we choose the filter angle $\theta_f = 0$ such that we focus on the single segmented region. The PSD for this case is shown in Fig. 28. Of all the unfiltered components we see that this filter configuration favours purely radial modes, when the amplitude of each mode is equal (case (a) in Fig. 28). The straight filter, as expected, is more restrictive and only allows a few of the modes seen in Fig. 27 to contribute to the measurement.

If instead, we orient the filter to focus on the double segmented regions, thus $\theta_f = 90$ degrees, we get the PSD as shown in Fig. 29. For a density fluctuation with uniform amplitude, this filter configuration seems to slightly favour $k_y\rho_i \sim 0.4$ in the wedge filter case, and $k_y\rho_i \sim 0.1 - 0.2$ in the straight filter case. For the actual GENE simulation we see that mainly $k_y \neq 0$ modes remain. These results for the single segmented and double segmented cases are in agreement with the results from the conceptual design of TPCI at JT-60SA[27]. There it was shown that the PCI measurement in the single segmented case essentially consists of the contribution from purely radial modes while the direction of $k_{\perp,B}$ is less constrained in the double segmented case.

To estimate the localisation we apply the same method as in Section IV for a given k_x and k_y component. The integration, Eq (21), is performed separately around each value of $\ell_\perp(k_x, k_y)$ to compute the contribution from either the double

segmented regions, or the single segmented region. Due to the multiple values of $\ell_\perp(k_x, k_y)$ it is much more challenging to compute the localisation as it is difficult to properly distinguish the different segments from each other. To simplify we therefore limit the analysis to the unfiltered and straight filter configuration only. The latter yields in fact the optimal localisation that can be achieved in JT-60SA. Furthermore we relax the criterion in Eq. (22) and choose ε such that the combined power from the different segments is at least 70% of the PSD when integrating over the full laser beam length (instead of 90 % as was used for TCV). If ε is too large we otherwise, wrongly, end up connecting the different segments together. Finally, we also limit the analysis to the 6 smallest k_y modes considered in the simulation, $k_y\rho_i = 0, 0.1, 0.2, 0.3, 0.4$ and $k_y\rho_i = 0.5$. Finally, we limit the integration length around each segment to ~ 2 m, again to avoid connecting the different segments together.

We group the localisation into the three following categories: single segmented region with $\ell_\perp \in [2.5, 5]$ m as seen in Fig. 26, the first double segmented region with $\ell_\perp \in [1, 1.5]$ m and finally, the second double segmented region, $\ell_\perp \in [5.5, 6.5]$ m. As was mentioned before, $\theta_{k_{\perp,B}, k_0}$ has a sharp variation in the two double segmented regions. To properly satisfy the criterion $k_{\text{meas}} \perp k_0$ we need sufficiently large values of $k_{\perp,B}$ that the phase in Eq. (23) varies more rapidly than the variation of $\theta_{k_{\perp,B}, f}$ and $\theta_{k_{\perp,B}, k_0}$ in the double segmented regions. In the current GENE simulation of JT-60SA the largest value $k_{\perp,B}$ is still too low and we therefore discard the double segmented regions from the analysis in the unfiltered cases. However, it is still possible to include them in the analysis of the straight filtered cases, as will be done later

The localisation for the single segmented region, in terms of $\Delta\rho_{k_x, k_y}$ for the unfiltered and straight filtered cases, is shown in Fig. 30. As before, the unfiltered case tests the property $k_{\text{meas}} \perp k_0$. In the case of a density fluctuation of the form of Eq. (23), (top plot, a) we see that this property is well satisfied for large enough values of k_x, which corresponds to larger values of $k_\perp$. We find very good localisation for $k_\perp > 5$ cm^{-1} with $\Delta\rho_{k_x, k_y} < 0.1$. At lower values of $k_\perp$ most components saturate at $\Delta\rho_{k_x, k_y} \approx 0.35$ which corresponds to the maximum value of $\Delta\rho_{k_x, k_y}$ corresponding to the maximum integration length $\Delta L_{k_x, k_y} \sim 2$ m considered in the analysis. The actual integration length for the low values of $k_\perp$ might actually be longer. There is a slight spread in the localisation due to imprecision of the underlying algorithm. We therefore include a cubic spline fit, with tension, through the points (solid lines) to more clearly illustrate the integration length at each value of $k_\perp$.

In the next step we apply the straight filter, using 0 degree filter angle so that we only capture contributions to the PCI measurement from the single segmented region. We see that we clearly mainly get contributions from very low k_y type modes, as the larger values of k_y lead to negligible contributions and are therefore not shown. The localisation for the remaining low k_y components is very similar to the corresponding result in the unfiltered case, with very good localisation for $k_\perp > 5$ cm^{-1}. This means that the averaging effect from the integration in fact is more restrictive compared to the size of
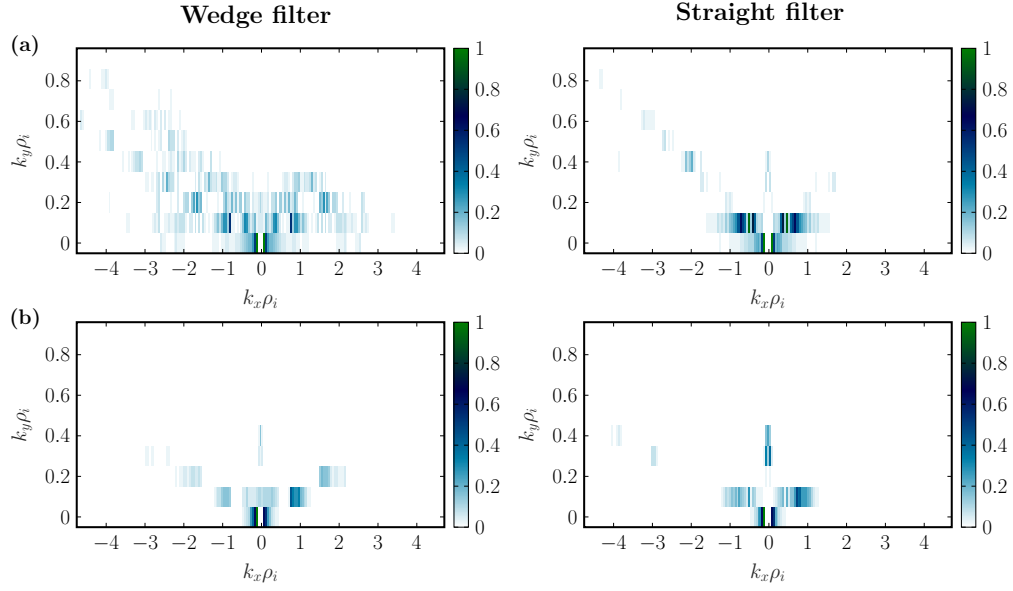
FIG. 28. PSD of each k_x, k_y component when integrating over the full JT-60SA laser beam path, when applying a 30 degree wedge filter (left column) or a straight filter (right column). The top row (a) shows the effect of the phase θ only, thus a density fluctuation of the form of Eq. (23) while the bottom row (b) shows the actual simulated case, using Eq. (27). Here the filter orientation is $\theta_f = 0$, focusing on the single segmented region. Only k_x, k_y modes with a connection are shown whereas the other components are set to zero.
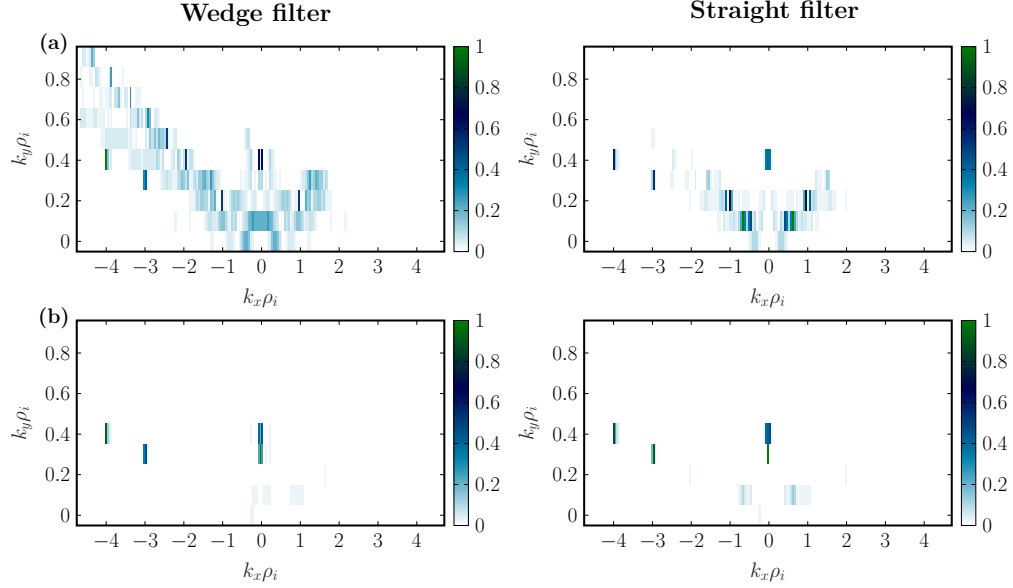
FIG. 29. Same as 28 but with $\theta_f = 90$ degrees, thus focusing on the double segmented regions.

the filter. That is, a fluctuating component is being averaged out sooner than it falls outside the filter.

If we use the actual form of the density fluctuation we get the corresponding results for the unfiltered and the filtered cases, shown in the third (c) and fourth row (d) in Fig. 30 respectively. We can see that only a few fluctuating components have a non-negligible contribution to the PCI measurement, and these components have relatively low values of $k_\perp$ and are therefore poorly localised. Normally components with higher

k_x have lower amplitudes which explains the low $k_\perp$ values of the components that remain in the two bottom plots in Fig. 30.

We then rotate the filter and use a filter angle $f_a = 90$ degrees to focus instead on the two double segmented regions. The corresponding localisation for these cases is shown in Fig. 31. The top row shows the case of a density fluctuation of the form of Eq. (23) while the bottom row shows the case when including the actual simulated density fluctuations.
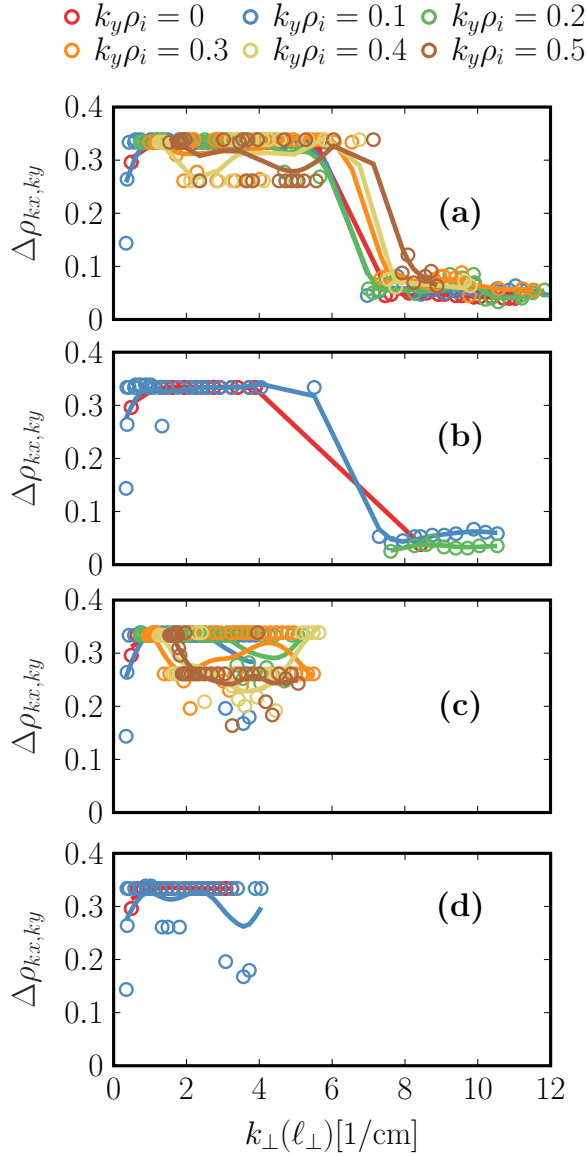
FIG. 30. Localisation in terms of the radial coordinate $\Delta\rho_{k_x,k_y}$, in JT-60SA, after applying Eq. (21) and using the criterion in Eq. (22) for the components. The localisation is shown for 6 different values of the binormal wave number $k_y\rho_i$ (circles) and a cubic spline fit (solid lines) is shown to more clearly illustrate the integration lengths. The localisation is shown for the case of a density fluctuation of the form of Eq. (23), (a,b) and when including the actual simulated density fluctuations (c,d). We show the unfiltered cases (a,c) and the cases when we apply the straight filter (b,d), using a 0 degree filter angle to focus on the single segmented regions.

Due to the very fast rotation of the wave vector of the fluctuations, the fluctuations quickly fall outside the narrow straight filter and are consequently very well localised. Already for $k_\perp > 1$ cm^{-1} we have a very small integration length with $\Delta\rho_{k_x,k_y} < 0.1$. The localisation in the second double segment is slightly better compared to the first double segment. In contrast to the single segmented case, the double segmented re-

gions include contributions from larger values of k_y, as was already shown in Fig. 29. Just as in the case of the single segmented region in Fig. 30, when considering the actual GENE-simulated case, Eq. (27), we see that fewer components remain, and these components have lower values of $k_\perp$. However, unlike the single segmented region, due to the fast rotation of the wave vector of the fluctuations, these components remain very well localised. The only exception are some very large scale modes with $k_\perp < 0.5$ cm^{-1} that have $\Delta\rho_{k_x,k_y} > 0.5$ in the first double segmented region.

To conclude, we find that in the single segmented region we obtain well defined segments that are mainly defined by how rapidly a fluctuating k_x,k_y component is being averaged out, due to the line integration. We also have a well defined direction of the wave vector, mostly purely radial, that contributes to the measurement. When the filter is oriented to mostly focus on the fluctuating contribution from the two double segments instead, the localisation is achieved purely by how fast a given k_x,k_y component falls outside the spatial filter. Due to the rapid variation of $\theta_{k_{\perp,B,f}}$ in the double segmented regions, as seen in Fig. 26 (c), the $k_\perp$ values in the present GENE simulation are too to small to be able to see an effect due to the line average of the fluctuations. The contribution now is dominated by poloidal modes $k_y \neq 0$ rather than $k_y = 0$. We should again stress that these estimates of the localisation, obtained using a local simulation with the flux tube centred at one radial position, are by no means final. A more proper estimate of the localisation could be performed with a global simulation that would take into account the radial variation in the phases and amplitudes of the fluctuations. This, however, was outside the scope of this paper, but is planned for future work. The equations presented in this paper are fully applicable also to a global case when using the Gaussian beam approach described in subsection III B 1. The plane wave approach described in subsection III B 2 can also be applied after estimating the k_x wave numbers. If we look back at the definition of the perpendicular wave number in eq. (20) we see that in a tokamak only k_y corresponds to an exact mode number while k_x follows from the periodic boundary conditions used in the flux tube representation. In experiments, however, k_x can be estimated by computing $k_{x,\text{eff},\ell_\perp}$, for example by computing the local radial correlation length at a given poloidal angle χ. From the knowledge of the magnetic shear and the toroidal mode number of the considered mode one could then use the relationship, $k_{x,\text{eff}}(\ell, r) = k_x + \chi(\ell)\hat{s}k_y$ to infer k_x. This would also be the approach to generalise the equations shown here for a global gyrokinetic simulation, and to potentially establish a link between the k_x representation and the radial correlation length measured in experiments.

Finally, we will compute the actual synthetic signals for the two filter orientations and make a first prediction of the turbulence measurement with PCI at JT-60SA. However, since we are already very limited in the number of components in the GENE fluctuations we will use a 30 degree wedge filter instead of the narrow straight filter that otherwise would lead to very low signal levels. The conditional spectra for the two filter orientations are shown in Fig. 32. For both filter orientations we see two narrow legs that are essentially straight,
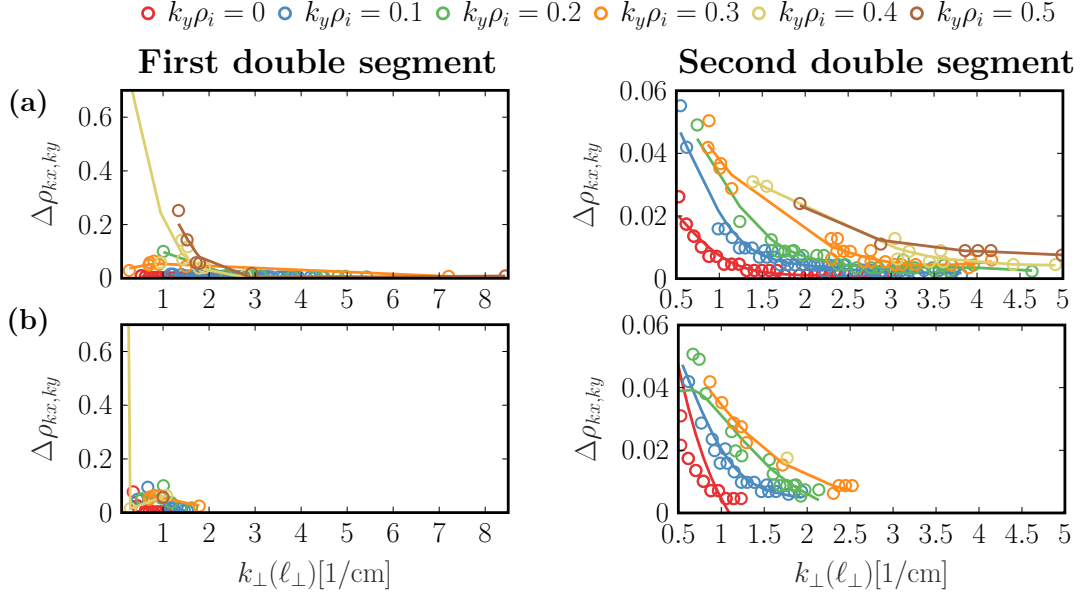
FIG. 31. Localisation in terms of the radial coordinate $\Delta\rho_{k_x,k_y}$, in JT-60SA, after applying Eq. (21) and using the criterion in Eq. (22) for the components. Only the results when we apply the straight filters are shown, using a 90 degree filter angle to focus on the first (left column) and second (right column) double segmented regions. The localisation is shown for 6 different values of the binormal wave number $k_y\rho_i$ (circles) and a cubic spline fit (solid lines) is used to more clearly illustrate the integration lengths. The localisation is shown for the case of a density fluctuation of the form of Eq. (23), (top row, a) and when including the actual simulated density fluctuations (bottom row, b).

which indicates a large phase velocity $\Delta F/\delta k_r$ of the measured fluctuations. The legs are slightly wider in the double segmented case compared to the measurement in the single single segment near the HFS edge.

The corresponding wave number spectrum is shown in Fig. 33. We see that the signal amplitudes are essentially similar for both filter orientations. However, clearly the single segmented case has a higher contribution from the purely radial fluctuating components while the double segmented case is more dominated by modes with $k_y \neq 0$. This is in agreement with the PSD levels seen already in Fig. 28 and Fig. 29

VI. SUMMARY AND CONCLUSIONS

In this paper we have presented the details of a synthetic diagnostic that models measurement with PCI by postprocessing electron density fluctuations generated by gyrokinetic simulations. In its present state it uses GENE simulations but can easily be adapted also to other gyrokinetic codes. An important novel feature included in the synthetic PCI is the possibility to apply a filter in wave-number space. This filter selects the measured wave vector direction and this translates into a longitudinal localisation of the signal in space. Such a filter must be taken into account when modelling PCI measurements on TCV, and in the future also on JT-60SA. We implemented two different versions of the synthetic diagnostic. The first properly takes into account the Gaussian form of the PCI laser beam which is required to accurately compute the synthetic PCI signals. We also considered a simplified ap-
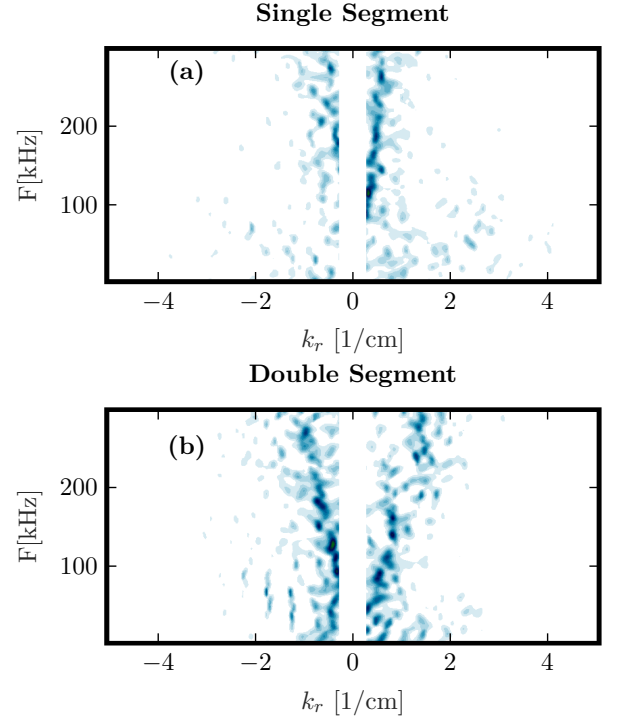

FIG. 32. The conditional spectrum calculated for the JT-60SA TPCI measurement, when using a wedge filter with a 30 degree half angle, with $\theta_f = 0$ thus focusing on the single segmented region (a) or $\theta_f = 90$ degrees that focuses on the double segmented regions instead (b).
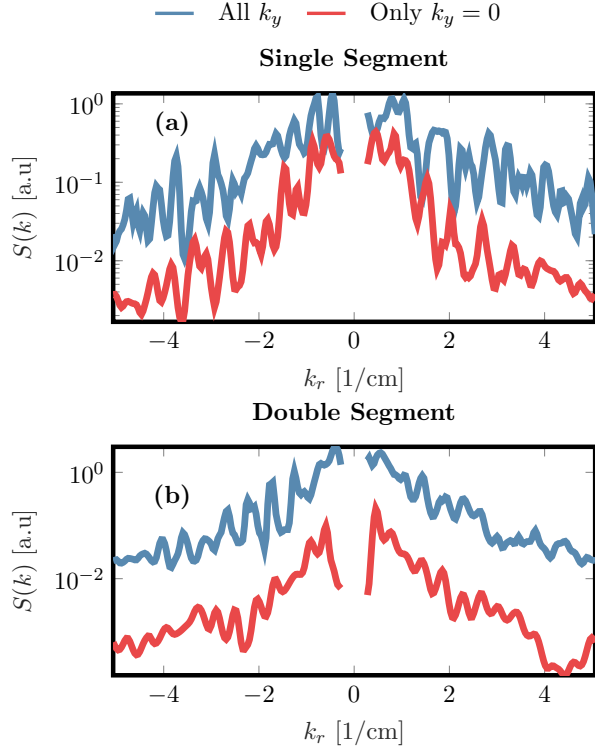
FIG. 33. Synthetic JT-60SA wave-number spectrum for the single segmented case (a) and the double segmented case (b) The result is shown when including all k_y contributions in Eq. (16) (blue) and only $k_y = 0$ (red).

proach, approximating the PCI laser beam as an infinite plane wave which allowed us to write the synthetic signals in terms of the GENE k_x and k_y modes. Using the plane wave approximation we have shown from first principles how the spatial filters affect the PCI signals and the localisation we obtain for different k_x and k_y modes. In general we find that the localisation is good for large enough $k_{\perp,B}$ but not as good as was predicted from simplified analytical considerations.

We then performed a comparison between experimental and synthetic results for positive and negative triangularity TCV discharges and found good qualitative agreement. We concluded that the change in propagation direction when changing the sign of the triangularity is due to a change in the characteristics of the fluctuations, particularly the GAM, as well as the effect of measurement geometry. Finally, we also analysed the localisation properties of PCI on JT-60SA and made first predictions for PCI measurements, which in the future might be compared with experiments.

ACKNOWLEDGMENTS

Appendix A: The parallel boundary condition[7,21]

For any fluctuating quantity Φ, for example the electrostatic potential, GENE considers coupled radial k_x modes

$$\Phi(k_x, k_y, z + 2\pi) = \Phi(k_x + 2\pi k_y \hat{s}, k_y, z),$$

which reflects poloidal periodicity in a toroidal system which in real space reads

$$\Phi(x, y, z + 2\pi) = \Phi(x, y - 2\pi C_y q(x), z). \quad (A1)$$

However, this periodicity is exactly ensured only when considering a radial shift Δx in the safety factor profile

$$q(x) = q_0 \left(1 + \hat{s}\frac{x - \Delta x}{r_0}\right) = q_0 \left(1 - \hat{s}\frac{\Delta x}{r_0}\right) + \frac{\hat{s}x}{C_y}, \quad (A2)$$

which can be seen as follows. From the definition of the binormal coordinate in Eq. (8) and by representing a fluctuating quantity $\Phi(x, y, z)$ in Fourier space and using the parallel boundary condition in Eq. (A1) we obtain

$$\Phi(x, y, z + 2\pi)$$
$$= \sum_{k_x} \sum_{k_y} \Phi(k_x, k_y, z) e^{ik_x x} e^{ik_y \left(y - C_y 2\pi q(x)\right)}$$
$$= \sum_{k_x} \sum_{k_y} \Phi(k_x, k_y, z) e^{ix\left(k_x - k_y 2\pi \hat{s}\right)} e^{ik_y y} e^{-ik_y C_y 2\pi q_0 \left(1 - \hat{s}\frac{\Delta x}{r_0}\right)}$$
$$= \sum_{k_x} \sum_{k_y} \Phi(k_x + \hat{s}k_y 2\pi, k_y, z) e^{ik_x x} e^{ik_y y} e^{-ik_y C_y 2\pi q_0 \left(1 - \hat{s}\frac{\Delta x}{r_0}\right)},$$

where we find the familiar coupling between k_x modes $k_x' = k_x + k_y 2\pi \hat{s}$ as a consequence of the parallel boundary condition. GENE assumes that the remaining phase factor in the above equation is unity, and thus that $k_y C_y q_0 \left(1 - \hat{s}\Delta x/r_0\right) \in \mathbb{Z}$. This corresponds to choosing the radial shift such that

$$\Delta x = \frac{C_y}{n_0 \hat{s}} \left(\text{NINT}(n_0 q_0) - n_0 q_0\right), \quad (A3)$$

where $\text{NINT}(y)$ finds the nearest integer to y. Eq. (A3) in fact corresponds to shifting the origin of the simulation box to the nearest mode rational surface. Also, n_0 corresponds to the toroidal mode number. Note that in Eq. (A3) n_0 does not necessarily have to be an integer, meaning that the binormal wave numbers, $k_y = p n_0 / C_y$ for $p \in \mathbb{Z}$, considered in the simulation might not correspond to an integer toroidal mode number. We will therefore always have continuity in the parallel coordinate even if flux tube does not correspond to a rational fraction of a full toroidal turn.

[1] S. Coda, M. Porkolab, and T. N. Carlstrom, Review of Scientific Instruments **63**, 4974 (1992).

[2] S. Coda, Ph.D. Thesis, MIT Plasma Science and Fusion Center (1997).

[3] E. Nelson-Melby *et al.*, Phys. Rev. Lett. **90**, 155004 (2003).

[4] A. Marinoni, Ph.D. Thesis, EPFL (2009).

[5] K. Tanaka *et al.*, Review of Scientific Instruments **79**, 10E702 (2008).

[6] E. M. Edlund *et al.*, Review of Scientific Instruments **89**, 10E105 (2018).

[7] F. Jenko, W. Dorland, M. Kotschenreuther, and B. N. Rogers, Physics of Plasmas **7**, 1904 (2000).

[8] E. Highcock, Ph.D. thesis, University of Oxford, 2012.

[9] Gyrokinetic Simulations Project, `http://gyrokinetics.sourceforge.net/`, accessed: 2021-10-11.

[10] E. Lanti *et al.*, Computer Physics Communications **251**, 107072 (2020).

[11] A. Peeters *et al.*, Computer Physics Communications **180**, 2650 (2009), 40 YEARS OF CPC: A celebratory issue focused on quality software for high performance, grid and novel computing architectures.

[12] GENE web page, `http://genecode.org/`, accessed: 2018-04-25.

[13] T. Görler *et al.*, Journal of Computational Physics **230**, 7053 (2011).

[14] J. Candy and R. E. Waltz, Journal of Computational Physics **186**, 545 (2003).

[15] M. Fahey and J. Candy, in *SC '04: Proceedings of the 2004 ACM/IEEE Conference on Supercomputing* (PUBLISHER, ADDRESS, 2004), pp. 26–26.

[16] D. R. Ernst *et al.*, *Proceedings of the 21st IAEA Fusion Energy Conference*, Chengdu, China, 2006 (International Atomic Energy Agency, Vienna, 2006), TH/1-3 .

[17] J. C. Rost, L. Lin, and M. Porkolab, Physics of Plasmas **17**, 062506 (2010).

[18] N. Kasuya, M. Nunami, K. Tanaka, and M. Yagi, Nuclear Fusion **58**, 106033 (2018).

[19] H. Weisen, Review of Scientific Instruments **59**, 1544 (1988).

[20] C. A. Michael *et al.*, Review of Scientific Instruments **86**, 093503 (2015).

[21] G. Merlo, Ph.D. Thesis, EPFL (2016).

[22] H. Lütjens, A. Bondeson, and O. Sauter, Computer Physics Communications **97**, 219 (1996).

[23] F. Carpanese, Ph.D. Thesis, EPFL (2021).

[24] M. Pueschel, T. Dannert, and F. Jenko, Computer Physics Communications **181**, 1428 (2010).

[25] Z. Huang, S. Coda, and the TCV Team, Plasma Physics and Controlled Fusion **61**, 014021 (2019).

[26] C. A. De Meijere, Ph.D. Thesis, EPFL (2013).

[27] S. Coda *et al.*, Nuclear Fusion **61**, 106022 (2021).

[28] Z. Huang, Ph.D. Thesis, EPFL (2017).

[29] A. Marinoni, S. Coda, R. Chavan, and G. Pochon, Review of Scientific Instruments **77**, 10E929 (2006).

[30] Z. Huang and S. C. and, Plasma Physics and Controlled Fusion **61**, 014021 (2018).

[31] C. A. de Meijere *et al.*, Plasma Physics and Controlled Fusion **56**, 072001 (2014).

[32] F. I. Parra, M. Barnes, and A. G. Peeters, Physics of Plasmas **18**, 062501 (2011).